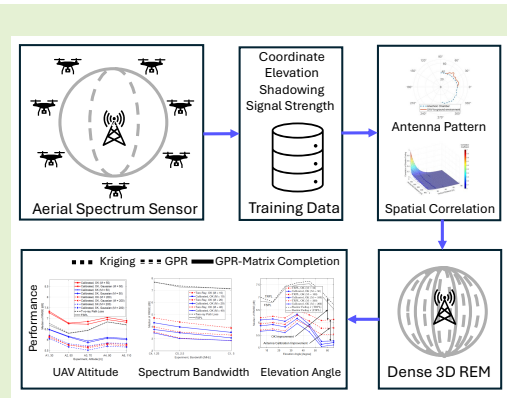


UAV-Based 3D Spectrum Sensing: Insights on Altitude, Bandwidth, Trajectory, and Effective Antenna Patterns on REM Reconstruction

Mushfiqur Rahman, *Graduate Student Member, IEEE*, Sung Joon Maeng, *Member, IEEE*, İsmail Güvenç, *Fellow, IEEE*, Chau-Wai Wong, *Senior Member, IEEE*, Mihail Sichitiu, *Member, IEEE*, Jason A. Abrahamson, and Arupjyoti Bhuyan, *Senior Member, IEEE*

Abstract—Spectrum sensing and the generation of 3D Radio Environment Maps (REMs) are essential for enabling spectrum sharing within cognitive radio networks. While Uncrewed Aerial Vehicles (UAVs) offer high-mobility 3D sensing, REM accuracy is challenged by dynamic flight behaviors, where fluctuations in UAV speed and direction introduce measurement inconsistencies. Furthermore, the structural influence of the airframe itself impacts the onboard antenna's radiation characteristics. In this paper, we present a comprehensive analysis of REM reconstruction at various altitudes, using real-world data from a fixed base station tower and a ground-vehicle source. We evaluate diverse reconstruction methodologies, including Kriging (simple, ordinary, and trans-Gaussian), matrix completion, and Gaussian process regression (GPR) for recovery from sparse samples. Our results indicate that simple Kriging and GPR remain more robust under extreme sample sparsity. Additionally, we propose a special framework to enhance reconstruction accuracy in deep-shadowed regions by decomposing the REM into distinct smooth and deep-shadowed spatial components. We further investigate how REM reconstruction performance is influenced by physical and UAV-related external parameters. First, we demonstrate that the impact of UAV altitude on accuracy follows a tri-phasic trend: an initial performance gain up to h_1 , a performance dip between h_1 and h_2 , and a final stage of increasing accuracy. Additionally, we show that performance improves with increased spectrum bandwidth. Second, our analysis of UAV trajectories reveals that the variance of shadow fading exhibits a non-monotonic trend, peaking at both very low and mid-high elevation angles. Finally, we demonstrate that antenna pattern calibration from in-field measurements significantly enhances REM reconstruction accuracy by accounting for electromagnetic interference and shadowing induced by the UAV airframe.

Index Terms—3D spectrum sensing, air-to-ground, antenna pattern calibration, Gaussian process regression (GPR), Kriging, matrix completion, radio environment maps (REM), shadow fading, spatial correlation, UAV.



I. INTRODUCTION

THE rapid expansion of wireless ecosystems, spanning terrestrial and aerial domains, has necessitated a fundamental shift in how spectral resources are perceived and managed. As the density of diverse transmitters, including femtocells, Internet of Things (IoT) devices, 5G-enabled vehicles, and Uncrewed Aerial Vehicles (UAVs), continues to surge, the 3D spectrum environment has become increasingly congested [1]. Consequently, this complexity precipitates a critical state of spectrum scarcity where traditional static allocation models fall short of meeting the demands of modern connectivity. To address these challenges, cognitive radio technology leverages intelligent spectrum management strategies, such as dynamic

spectrum sharing, which relies on comprehensive, real-time awareness of spectrum occupancy [2]. Central to this awareness is the 3D Radio Environment Map (REM), a spatial database that characterizes received power levels, such as Reference Signal Received Power (RSRP), across specific coordinates and altitudes. Constructing a dense, high-fidelity 3D REM is therefore a foundational requirement for optimizing power control and frequency allocation while ensuring interference mitigation in a multi-layered wireless landscape.

Constructing a comprehensive 3D REM begins with the acquisition of RSRP measurements across diverse spatial locations. As exhaustive sampling is physically prohibitive, the process of REM generation relies on predictive strategies, such as spatial interpolation and channel modeling, to estimate signal levels in unobserved regions [3]. Recent advancements in REM reconstruction [3]–[10] have increasingly leveraged UAVs to facilitate these measurements, utilizing both fixed and autonomous trajectories in 3D environments. GPS-integrated,

© 2026 IEEE. Personal use permitted. Submitted to IEEE Sensors Journal. Copyright may be transferred without notice. (Corresponding author: İsmail Güvenç.)

Please see the Acknowledgment section of this article for the funding and author affiliations.

lightweight UAVs provide the agility required to navigate challenging terrains and precisely reach high-altitude coordinates that are inaccessible to ground-based infrastructure. Furthermore, the literature has explored sophisticated trajectory planning algorithms designed to enhance REM fidelity while minimizing operational overhead, such as flight time [5]–[7]. These approaches often employ Bayesian uncertainty metrics or deep learning frameworks to direct UAVs toward the most informative sampling locations, effectively prioritizing areas with high spatial variance or significant shadowing.

Despite the distinct advantages of UAV-assisted sensing, several platform-specific challenges complicate the acquisition of reliable data. First, real-world UAV measurements are inherently susceptible to diverse noise sources, including electromagnetic interference from rotors and onboard electronics, which are compounded by environmental shadowing and multi-path fading; consequently, reconstruction methods validated solely on statistical or ray-tracing-based synthetic data may not accurately reflect performance in practical deployments. Second, the spatial correlation of measurements is heavily influenced by the flight path; for instance, traversing the same trajectory from opposite directions or at varying speeds can yield significant signal variations due to changes in UAV orientation and heading. These kinematic factors, combined with the typically limited nature of real-world datasets, necessitate rigorous validation protocols tailored specifically for UAV-based sensing. Finally, the physical airframe of the UAV can significantly alter the antenna’s radiation characteristics compared to its baseline performance in an anechoic chamber, introducing gain distortions.

While extensive research has focused on data-driven reconstruction algorithms and path optimization for UAV-based sensing, limited effort has been dedicated to gaining fundamental insights into how physical and platform-related parameters affect REM fidelity for a known signal source. Leveraging real-world measurements for 3D REM slice reconstruction, this work addresses existing gaps through the following contributions:

- We demonstrate that REM reconstruction accuracy follows a tri-phasic function of altitude.
- We characterize a tri-phasic trend in shadowing variance, which peaks at low elevation angles due to ground-level clutter and again at mid-high angles where the line-of-sight (LoS) component from the antenna is strongest.
- We show that REM reconstruction accuracy improves with increased bandwidth due to frequency diversity, which reduces signal vulnerability to multipath fading.
- We evaluate the reconstruction performance of simple Kriging (SK), ordinary Kriging (OK), trans-Gaussian Kriging, and Gaussian Process Regression (GPR). Our results demonstrate that GPR delivers the best results.
- We propose a novel reconstruction framework, termed matrix completion (MC)-assisted GPR, specifically engineered to characterize radio environments dominated by localized deep-shadowing effects.
- We improve reconstruction performance by incorporating calibrated antenna patterns derived from real-world measurements, supplemented by standard gain patterns for

directions lacking empirical data.

The rest of the paper is organized as follows. Section II reviews the related literature on REM reconstruction techniques. Section III establishes the system model that will serve as the foundation of our analysis. Section IV describes the datasets. Section V introduces the complete end-to-end REM reconstruction algorithm. Section VI presents the antenna pattern calibration model. Section VII demonstrates the experimental results, and the final section concludes the paper.

II. RELATED WORK

This section first reviews the evolution of reconstruction methodologies from traditional data-driven interpolation to modern hybrid frameworks. We then examine the existing literature on altitude-dependent REM reconstruction and UAV airframe-induced antenna distortions.

A. REM Reconstruction Methodologies

The reconstruction of REMs from sparse UAV-collected measurements remains a significant research challenge. Existing literature generally categorizes these methodologies into three primary frameworks: direct, indirect, and hybrid reconstruction techniques [28].

Direct REM Reconstruction Methods treat the problem as a generic data interpolation or tensor completion task, without incorporating the underlying physics of radio propagation. This category includes classical spatial interpolation methods such as Kriging [29], Inverse Distance Weighting (IDW), and Gaussian Process Regression (GPR). GPR is typically implemented in two forms: 1) *spatial GPR*, which is mathematically analogous to Kriging [24], and 2) *feature-based GPR*, which utilizes variables such as 3D distance, azimuth, and elevation to predict received power [27]. In this paper, we employ the first form of GPR, which extends simple Kriging by explicitly modeling measurement noise as a Gaussian process. The efficacy of Kriging and spatial GPR depends on the covariance kernel, which models spatial signal correlation. Common kernel selections include a family of exponential, Matern, and sinusoidal exponential functions. While kernel hyperparameters are traditionally estimated from sampled data, calibrating them in a controlled anechoic chamber has also been proposed [30], as data anomalies can hamper their performance [31], [32].

Deep Learning (DL) models have gained traction due to their superior generalization capabilities, despite the requirement for extensive training datasets [10], [23], [33], [34]. Current DL architectures for REM generation primarily utilize U-Net [12], [13], autoencoders [14], [21], Generative Adversarial Networks (GANs) [19], [22], or diffusion models [26]. These methodologies are further divided into *sampling-free* approaches, which rely solely on transmitter (Tx) locations and environmental metadata (e.g., terrain or building maps) as their input, and *sampling-based* approaches that integrate sparse measurements. This work specifically addresses scenarios involving known Tx locations and limited sampled measurements. Notably, most of the state-of-the-art DL methods are trained and validated on synthetic data rather

TABLE I: Literature review of radio environment map reconstruction.

Literature (First author <i>et al.</i> , year)	Method	Input (Tx Location, Observations)	Multi- altitude	Multi- bandwidth	UAV-based measurements	Elevation dependency	Radiation calibration
Pesko (2015) [11]	Okumara-Hata	✓ ✓	✗	✗	✓	✗	✓
Krijestorac (2021) [12]	U-Net	✗ ✓	✗	✗	✗	✗	✗
Levie (2021) [13]	U-Net (RadioUnet)	✓ ✓	✗	✗	✗	✗	✗
Teganya (2021) [14]	Autoencoder	✗ ✓	✗	✗	✗	✗	✗
Mao (2022) [15]	BPNN, GAN	✓ ✓	✗	✗	✓	✗	✗
Sun (2022) [16]	MC	✗ ✓	✗	✗	✗	✗	✗
Liu (2023) [17]	RT, Kriging	✓ ✓	✗	✗	✗	✗	✗
Maeng (2023) [18]	TRPL, Kriging	✓ ✓	✗	✗	✓	✗	✗
Hu (2023) [19]	GAN	✗ ✓	✓	✗	✗	✗	✗
Ivanov (2023) [20]	IDW, Kriging	✗ ✓	✓	✗	✓	✗	✗
Locke (2023) [21]	Autoencoder	✓ ✓	✗	✗	✗	✗	✗
Zhang (2023) [22]	GAN (RME-GAN)	✓ ✓	✗	✗	✗	✗	✗
Chaves (2023) [23]	U-Net, cGAN	✗ ✓	✗	✗	✗	✗	✗
Zeng (2023) [10]	CNN	✓ ✓	✗	✗	✗	✗	✗
Wang (2024) [24]	SBL, GPR	✓ ✓	✓	✗	✗	✗	✗
Rahman (2024) [25]	TRPL, Kriging, MC	✓ ✓	✗	✗	✓	✗	✗
Wang (2024) [26]	Diffusion (RadioDiff)	✓ ✗	✗	✗	✗	✗	✗
Alobaidy (2025) [27]	SLR, EBT, GPR	✗ ✓	✓	✗	✓	✗	✗
This paper	TRPL, GPR, MC	✓ ✓	✓	✓	✓	✓	✓

than in-field UAV measurements. A recent study identified the U-Net architecture as the top-performing model, utilizing the extensive *SpectrumNet* simulated radio map dataset for benchmarking [35]. Finally, matrix completion [16], [36] leverages low-rank characteristics to predict unknown grid values. While reliable for single-source scenarios, its performance often degrades due to oversmoothing in multi-source or deep-shadowing environments [37].

Indirect REM Reconstruction Methods leverage the physics of radio propagation by assuming a deterministic propagation model, such as log-distance or two-ray path loss, and estimating model parameters from observed samples. These methods are termed “indirect” because the REM is generated via a tuned channel model. The process involves estimating variables such as the path loss exponent, LoS probability, shadow fading variance, source location, and antenna radiation patterns [28], [38]. While pure modeling (e.g., ray-tracing) can be performed without measurements, indirect methods utilize sparse samples to adapt the model to specific site characteristics. For instance, Pesko *et al.* [11] utilized the Okumura-Hata model to estimate source location and tune Tx antenna patterns via non-linear optimization. Other studies address source localization and parameter estimation using Orthogonal Matching Pursuit (OMP) [39] or Sparse Bayesian Learning (SBL) [1]. While these approaches eliminate the need to store large volumes of sparse samples, their accuracy is inherently limited by how well the chosen channel model reflects the underlying RF distribution of the real-world environment.

Hybrid Methods bridge the gap between direct and indirect frameworks. While direct methods are model-agnostic, indirect methods provide physical grounding; a hybrid approach typically yields superior accuracy by combining these strengths [3], [40]. For example, Mao *et al.* employed a geometric propagation model to identify multipath delays, subsequently using a machine learning model to predict indi-

vidual path powers. Similarly, Liu *et al.* modeled deterministic path loss using environmental semantics and estimated residual shadow fading via Kriging. Likewise, Maeng *et al.* employed two-ray path loss and Kriging. In our work, we adopt the two-ray path loss model with GPR. Given that the transmitter location is known, we first utilize the two-ray model to establish the large-scale path loss trend. Subsequently, we model the residual shadow fading through GPR to capture localized environmental characteristics that are otherwise difficult to characterize through purely physics-based models.

B. Altitude-Dependent REM Reconstruction

Ivanov *et al.* [20] evaluated Kriging and IDW performance across four distinct UAV altitudes. Although the authors did not explicitly analyze the altitude-dependency of their results, a secondary analysis of their data reveals a distinct tri-phasic trend: for both methodologies, the REM reconstruction error initially decreases as the altitude rises from 80 m to 90 m, undergoes a localized increase at 100 m, and subsequently decreases at 110 m. Maeng *et al.* [18] analyzed REM reconstruction error using multi-altitude UAV data by varying the vertical separation between training and testing sets (i.e., altitude offsets of 0 m, 10 m, and 20 m). Our objective diverges from [18] in that we investigate the intrinsic difficulty of intra-altitude prediction at each specific height layer, whereas the focus in [18] was to quantify the degradation in accuracy as the vertical distance between training and testing data increases.

C. Airframe-Induced Radiation Pattern Distortions

Recent studies [41]–[43] experimentally demonstrated that the radiation pattern of the antenna gets significantly altered when attached to a UAV, primarily due to uneven reflections and scattering, which introduce additional multipath components. Similarly, Sun *et al.* [44] showed that the UAV wings

can cause airframe shadowing, particularly at low elevation angles, such as when the UAV is slightly tilted, blocking the direct ray. Despite these known physical impairments, the impact of UAV-specific antenna pattern calibration on the accuracy of 3D REM reconstruction remains underexplored. While Pesko *et al.* [11] demonstrated that Tx antenna pattern calibration can effectively reduce reconstruction errors, their findings were based on simulated data. Furthermore, Maeng *et al.* [18] utilized anechoic chamber measurements to characterize the antenna in isolation; however, this approach does not account for the pattern distortion caused by the UAV airframe itself. While it is possible to measure the composite UAV-antenna pattern in a large-scale anechoic facility [43], in this work, we explore the feasibility of estimating the effective antenna pattern directly from in-field empirical measurements. This ensures the model captures the true interaction between the antenna and the UAV structure while in operation.

To the best of our knowledge, the dependence of REM reconstruction error on altitude, bandwidth, and elevation angle, alongside the integration of calibrated antenna patterns into a reconstruction framework using empirical UAV-collected data, remains insufficiently addressed in existing literature. Table I provides a comparative summary, highlighting the distinct contributions of this study relative to the current state-of-the-art in REM reconstruction.

TABLE II: Key abbreviations.

Abbreviation	Full name
APC	Antenna Pattern Calibration
BPNN	Back-Propagation Neural Network
BS	Base Station
GS	Ground Station
CNN	Convolutional Neural Network
EBT	Ensemble of Bagged Trees
FSPL	Free-Space Path Loss
GAN	Generative Adversarial Network
cGAN	Conditional Generative Adversarial Network
GPR	Gaussian Process Regression
IDW	Inverse Distance Weighting
LoS	Line of Sight
TRPL	Two-Ray Path Loss
MC	Matrix Completion
RT	Ray Tracing
REM	Radio Environment Maps
SBL	Sparse Bayesian Learning
SD	Standard Deviation
SF	Shadow Fading
SLR	Stepwise Linear Regression
Tx	Transmitter
Rx	Receiver
UGV	Unmanned Ground Vehicle

III. SYSTEM MODEL PRELIMINARIES

This section establishes the basis of the analytical framework for 3D REM reconstruction. We first characterize the radio environment through a physics-based path loss model and a stochastic formulation of shadow fading. Subsequently, we define the problem setup, which details the available system inputs, constraints, and the target reconstruction objectives.

TABLE III: Key variables in this study.

Symbol	Definition
θ	Elevation angle of the UAV
θ_t	Elevation angle of the LoS path at the GS
θ_r	Elevation angle of the LoS path at the UAV
ϕ_t	Azimuth angle of the LoS path at the GS
ϕ_r	Azimuth angle of the LoS path at the UAV
h_{uav}, H	Altitude of the UAV
h_{gs}	Altitude of the GS antenna
d_h	Horizontal distance between UAV and GS antenna
d_v	Vertical distance between GS and UAV antenna
d_{3D}	3D distance between UAV and GS antenna
l_{gs}	3D coordinate of the GS
l_{uav}	3D coordinate of the UAV
ψ_{uav}	Latitude of the UAV
ζ_{uav}	Longitude of the UAV
ψ_{gs}	Latitude of the GS
ζ_{gs}	Longitude of the GS
P_{Tx}	Transmit power (known)
P_{Rx}	Received power (measured)
\hat{r}_{trpl}	TRPL-estimated received power
$\hat{r}_{\text{trpl}}^{\text{(APC)}}$	TRPL-estimated received power with antenna pattern calibration
w_{trpl}, Z	SF component extracted as the RSRP residual relative to TRPL
$\sigma_Z, \sigma_w, \sigma$	Standard deviation of SF
R_w, R_Z	Spatial correlation of SF for a pair of locations
γ	Semivariogram of SF for a pair of locations
C	Covariance of SF for a pair of locations
l_0	3D coordinate of prediction location
\hat{w}	Estimated SF at prediction location
M	Number of sparse samples available
R	Sparse sample selection radius for Kriging
\hat{w}	Estimated SF recovered from sparse samples
\hat{r}	Reconstructed RSRP at unsampled locations
\mathcal{E}	Test dataset (with M sparse samples)
\mathcal{E}'	Auxiliary training dataset

A. System Environment and Radio Propagation Model

The spectrum sensing environment in this study consists of two nodes: a stationary ground-based node and a portable node equipped with a UAV. The stationary node may be either a base station (BS) or any other ground station (GS), with the Radio Frequency (RF) front-end and communication modules positioned atop. The ground-based node emits the radio signal while the UAV collects RSRP measurements to sense the surrounding radio environment. The communication modules are mounted beneath the UAV, with the antenna oriented downward. Both nodes are equipped with antennas featuring nearly omnidirectional radiation patterns, as detailed in their datasheets. To minimize interference from the frame structure (e.g., the UAV body) and other RF communication modules, both antennas are affixed to horizontal rods, creating separation from other components of the UAV or GS. The environment is assumed to be rural, featuring a LoS and a ground-reflected ray, as depicted in Fig. 1.

We define the 3D coordinates of the ground station antenna $l_{\text{gs}} = (\psi_{\text{gs}}, \zeta_{\text{gs}}, h_{\text{gs}})$ and the 3D coordinates of the UAV $l_{\text{uav}} = (\psi_{\text{uav}}, \zeta_{\text{uav}}, h_{\text{uav}})$, where ψ , ζ and h represent the latitude, longitude, and altitude, respectively. The horizontal and vertical distances between the ground station and the UAV

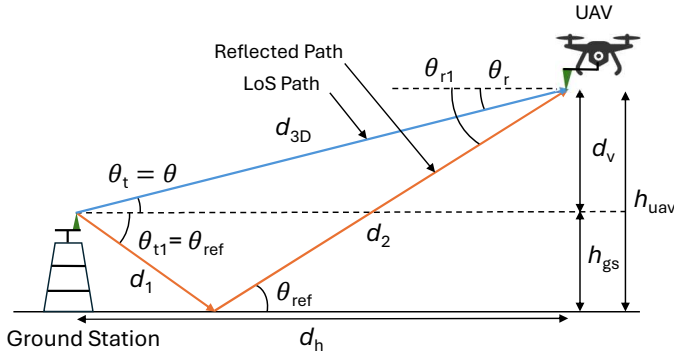


Fig. 1: Two-ray path loss (TRPL) model for a GS-to-UAV link with a horizontal rod mounted antenna.

are:

$$d_h(l_{gs}, l_{uav}) = R_e \cdot \arccos \left(\sin \psi_{uav} \sin \psi_{gs} + \cos \psi_{uav} \cos \psi_{gs} \cos(\zeta_{gs} - \zeta_{uav}) \right), \quad (1a)$$

$$d_v(l_{gs}, l_{uav}) = |h_{gs} - h_{uav}|, \quad (1b)$$

where R_e denotes the Earth's radius. The 3D distance, $d_{3D}(l_{gs}, l_{uav})$, is given by $\sqrt{d_h^2 + d_v^2}$. The two-ray path loss (TRPL) model calculates the signal attenuation factor by considering both the LoS and ground reflection paths as follows:

$$A_{\text{trpl}}(l_{gs}, l_{uav}) = \left(\frac{l_{\text{wave}}}{4\pi} \right)^2 \left| \underbrace{\frac{\sqrt{G_{gs}(\phi_t, \theta_t) G_{uav}(\phi_r, \theta_r)}}{d_{3D}}}_{\text{LoS signal}} + \underbrace{\frac{\Gamma(\theta_{\text{ref}}) \sqrt{G_{gs}(\phi_{t1}, \theta_{t1}) G_{uav}(\phi_{r1}, \theta_{r1})} e^{-j\Delta\tau}}{d_1 + d_2}}_{\text{ground reflected signal}} \right|^2, \quad (2)$$

where A_{trpl} represents the signal attenuation factor, defined as the ratio of the received power to the transmitted power. The terms $G_{gs}(\cdot)$ and $G_{uav}(\cdot)$ denote the antenna gain of the GS and UAV antennas, with their corresponding elevation and azimuth angles. The four elevation angles θ_t , θ_{t1} , θ_r , and θ_{r1} are demonstrated in Fig. 1. Additionally, l_{wave} is the wavelength, $\Delta\tau$ is the phase delay between two paths, and $\Gamma(\theta_{\text{ref}})$ is the ground reflection coefficient. The corresponding path loss, typically expressed on a dB scale, is given by:

$$PL_{\text{trpl}}^{(\text{dB})} = -10 \log_{10}(A_{\text{trpl}}). \quad (3)$$

The estimated received power using TRPL, denoted as \hat{r}_{trpl} , is given by:

$$\hat{r}_{\text{trpl}}^{(\text{dB})} = P_{\text{Tx}}^{(\text{dB})} - PL_{\text{trpl}}^{(\text{dB})}, \quad (4)$$

where $P_{\text{Tx}}^{(\text{dB})}$ is the transmit power in dB and $PL_{\text{trpl}}^{(\text{dB})}$ is the TRPL-estimated deterministic path loss given in (3).

B. Spatial Correlation of Shadow Fading

Unlike deterministic path loss, shadow fading (SF) follows a stochastic process characterized by spatial correlation across 3D space. This phenomenon, which captures large-scale fading caused by the presence of significant physical obstacles, varies

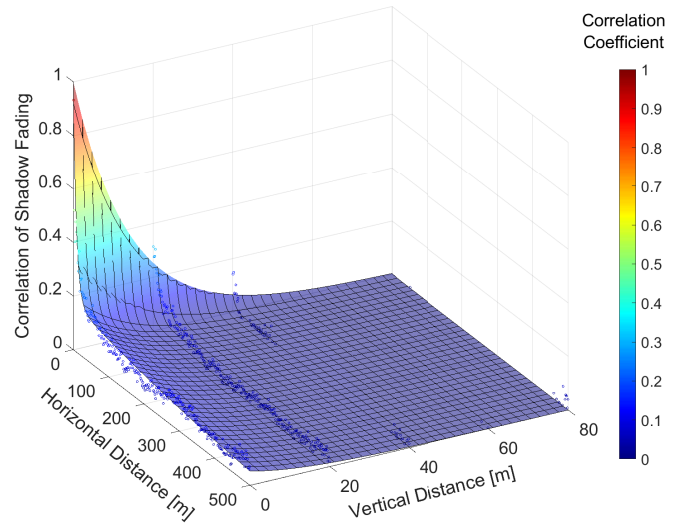


Fig. 2: Visualization of the spatial correlation of w as a function of the horizontal and vertical distances, d_h and d_v .

smoothly throughout the 3D environment [45]. Let w represent the SF component at a given location. For any two 3D coordinates, l_i and l_j , let d_h and d_v denote their respective horizontal and vertical separation distances. The spatial correlation of the SF between l_i and l_j , denoted by $R_w(l_i, l_j)$, is expressed as:

$$R_w(l_i, l_j) = \frac{\mathbb{E}[w(l_i)w(l_j)]}{\sigma_w^2}, \quad (5)$$

where $w(\cdot)$ represents the SF at the corresponding location and σ_w^2 denotes the variance of w . The spatial correlation $R_w(l_i, l_j)$ is characterized by exponential and biexponential distributions relative to the vertical distance d_v and horizontal distance d_h , respectively, as formulated in [18], [25]:

$$R_w(l_i, l_j) = e^{-qd_v} [ae^{-p_1 d_h} + (1-a)e^{-p_2 d_h}], \quad (6)$$

where a , p_1 , p_2 , and q are constants that can be estimated from field measurement data. An illustration of $R_w(l_i, l_j)$ with respect to d_v and d_h is provided in Fig. 2.

C. Problem Setup

To evaluate the performance of diverse reconstruction methodologies under a consistent framework and to investigate the influence of physical parameters, such as altitude, bandwidth, and elevation angle, on REM accuracy, we define a structured approach for independent 2D spatial plane estimation at fixed UAV altitudes. The problem is formulated as follows: for a given measurement campaign \mathcal{E} conducted at a constant altitude H , we have a set of n observed signal power data points. These measurements are denoted as $P_{\text{Rx}}^{(\text{dB})}(l_i)$, where $i \in \{1, \dots, n\}$, and l_i represents the 3D coordinate of the i -th measurement location. To simulate a **highly undersampled regime**, a small subset of M points is randomly selected from the n measurements to serve as the sparse samples for REM reconstruction. We vary M from 10 to 250 to analyze performance across various levels of data sparsity. The remaining $(n - M)$ points are reserved as a

ground-truth testing set to evaluate reconstruction accuracy at unsampled locations.

Furthermore, the transmitter location, the anechoic chamber antenna patterns of the isolated antennas, and the transmit power are provided. To facilitate parameter learning, a separate UAV campaign \mathcal{E}' , conducted at an altitude H' with n' measurements ($n' > M$), is utilized. This auxiliary dataset serves as the **training dataset** for estimating environmental spatial correlation parameters in (6) or for optimizing the weights of deep learning models, whereas the limited M samples from the target experiment \mathcal{E} are used during inference. To ensure a rigorous and valid train-test split, we maintain strict spatial separation between experiments \mathcal{E} and \mathcal{E}' . This is achieved by either ensuring a vertical separation ($|H - H'| \geq 20$ m) or by verifying that the 2D horizontal trajectories of \mathcal{E} and \mathcal{E}' are sufficiently disjoint when conducted at the same altitude.

IV. UAV MEASUREMENT DATASETS

This section first details the hardware configurations and experimental environments of the empirical UAV measurement datasets used in this study, and subsequently introduces each individual dataset along with its technical specifications.

A. Environment and Hardware Setup

In this study, we utilize three publicly available UAV-based RSRP measurement datasets [46]–[48], collected at one of the Aerial Experimentation and Research Platform on Advanced Wireless (AERPAW) [49], [50] experimentation sites located at the Lake Wheeler Field Labs in Raleigh, North Carolina, USA. A geographical map of the deployment environment is illustrated in Fig. 3(a). The UAV is equipped with an AERPAW portable node (APN), which integrates a Universal Software Radio Peripheral (USRP) and specialized RF frontends to function as a mobile spectrum sensor. Fig. 3(b) displays the UAV with the mounted APN, highlighting its core components. Specifically, a wideband antenna (SA-1400-5900) [51] is mounted on a horizontal rod beneath the UAV chassis. Across the datasets, two distinct ground station (GS) setups are employed: fixed base stations (BSs) equipped with RM-WB1-DN antennas [52], as shown in Fig. 3(c), and mobile APNs mounted on Uncrewed Ground Vehicles (UGV). The APNs utilize the same SA-1400-5900 antenna configuration, as depicted in Fig. 3(d).

B. Individual Datasets and Experiments

Table IV provides a short designation for all experiments used in this study, along with their respective properties.

1) *AERPAW LTE I/Q measurement dataset [46]*: A BS acted as the signal source, while the UAV collected I/Q samples at five different altitudes ranging from 30 m to 110 m, following a zigzag trajectory at each altitude. The resulting RSRP map is presented in Fig. 4.

2) *AERPAW Find-a-Rover (AFAR) dataset [47]*: The ground station was a UGV with an antenna height of 1.5 m above the ground. Across the five experimental campaigns in this dataset, the UAV flight altitudes ranged from 28 m to 47 m. The UAV trajectories were highly diverse, as illustrated in Fig. 5.

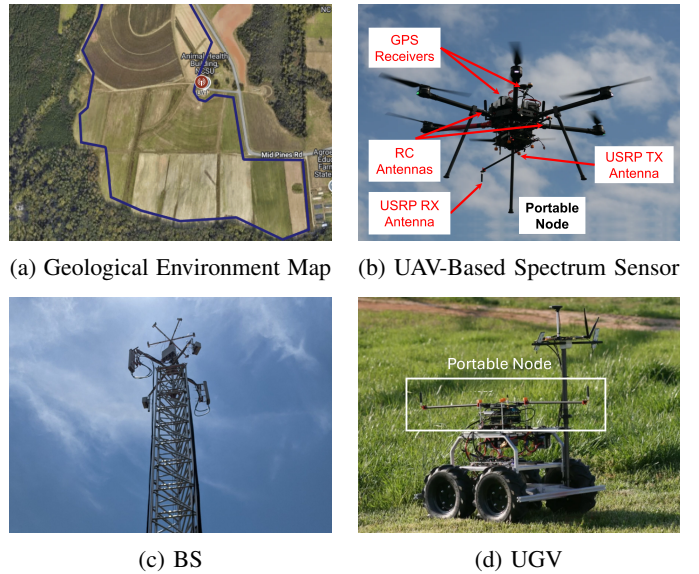


Fig. 3: Environment and communication nodes in the data collection setup: (a) Google Earth view of the site, (b) UAV-based measurement system, and (c) and (d) ground nodes.

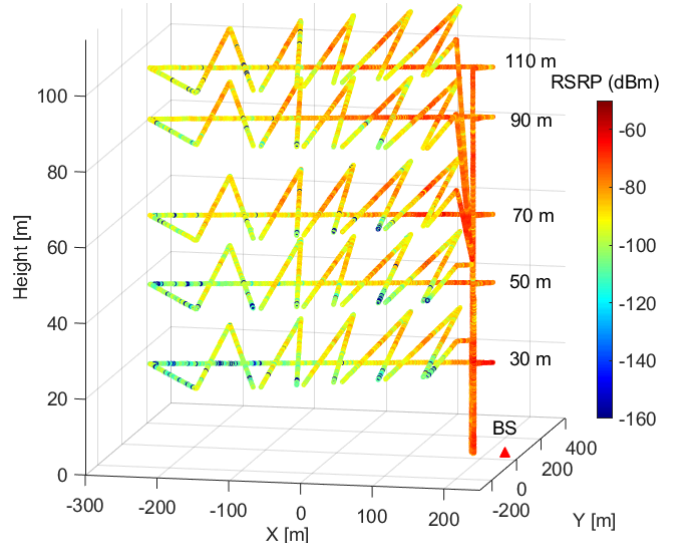


Fig. 4: AERPAW LTE I/Q measurement dataset [46].

3) *AERPAW multi-band dataset [48]*: The GS was the AERPAW BS, consistent with the AERPAW LTE dataset [46]. Data collection was conducted at UAV altitudes of 40 m, 70 m, and 100 m, with measurement bandwidths ranging from 1.25 MHz to 5 MHz. The resulting RSRP map for a representative bandwidth configuration is illustrated in Fig. 6.

V. 3D REM RECONSTRUCTION ALGORITHM

In this section, we present the 3D REM reconstruction framework, which integrates a deterministic radio propagation model for large-scale path loss prediction with a data-driven approach for stochastic component estimation. The reconstructed received power at an unsampled location, $\hat{r}^{(\text{dB})}$, is expressed on the dB scale as:

$$\hat{r}^{(\text{dB})} = \hat{r}_{\text{trpl}}^{(\text{dB})} + \hat{w}, \quad (7)$$

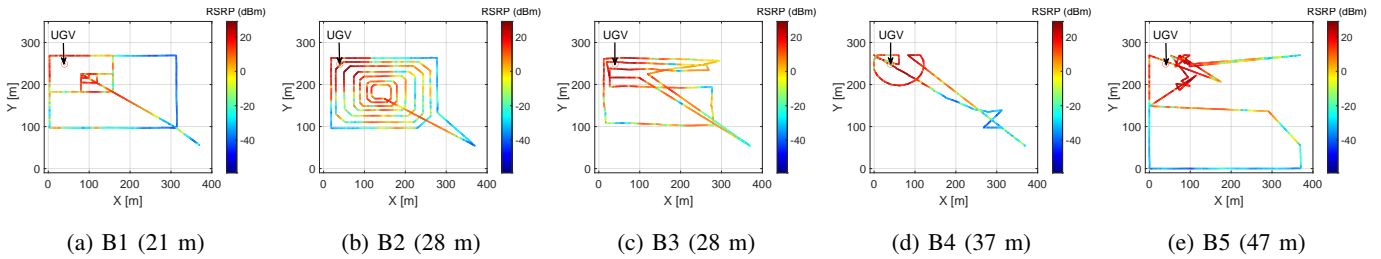


Fig. 5: AERPAW Find-a-Rover (AFAR) dataset [53], illustrating the UGV location and the UAV trajectories. The subfigure captions denote the specific experiment labels and their respective flight altitudes.

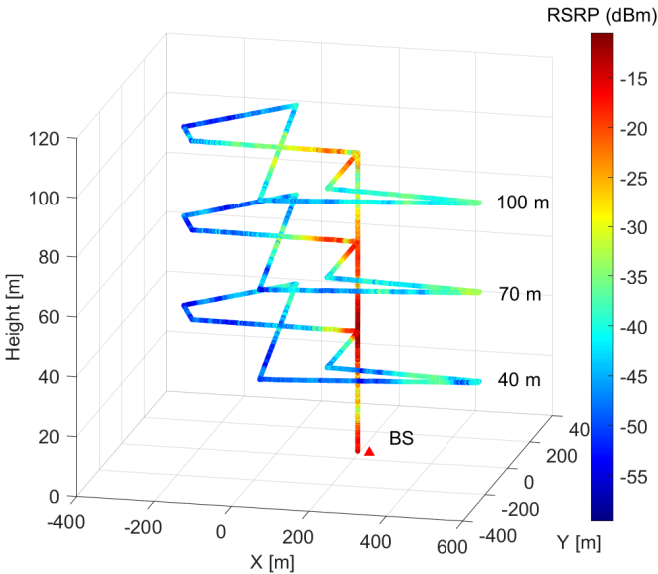


Fig. 6: Illustration of measured RSRPs at 5 MHz bandwidth for AERPAW multi-band dataset [48].

TABLE IV: Experiments considered in this study.

Dataset	Label	Altitude	Bandwidth	Carrier	GS
LTE I/Q	A1	30 m	1.4 MHz	3.5 MHz	BS
LTE I/Q	A2	50 m	1.4 MHz	3.5 MHz	BS
LTE I/Q	A3	70 m	1.4 MHz	3.5 MHz	BS
LTE I/Q	A4	90 m	1.4 MHz	3.5 MHz	BS
LTE I/Q	A5	110 m	1.4 MHz	3.5 MHz	BS
AFAR	B1	21 m	125 kHz	3.32 MHz	UGV
AFAR	B2	28 m	125 kHz	3.32 MHz	UGV
AFAR	B3	28 m	125 kHz	3.32 MHz	UGV
AFAR	B4	37 m	125 kHz	3.32 MHz	UGV
AFAR	B5	47 m	125 kHz	3.32 MHz	UGV
Multi-band	C1	40 m	5 MHz	3.3 MHz	BS
Multi-band	C2	70 m	5 MHz	3.3 MHz	BS
Multi-band	C3	100 m	5 MHz	3.3 MHz	BS
Multi-band	C4	40 m	1.25 MHz	3.3 MHz	BS
Multi-band	C5	40 m	2.5 MHz	3.3 MHz	BS

where $\hat{r}_{\text{trpl}}^{(\text{dB})}$ represents the predicted received power from the Two-Ray Path Loss (TRPL) model—calculated via (4) and \hat{w} is the predicted shadow fading (SF) derived from the data-

driven reconstruction techniques detailed hereafter.

These techniques utilize a subset of M sampled RSRP observations from a target experiment. By subtracting the TRPL-based received power from these observations, we isolate the M residual SF components, denoted as w_{trpl} , as follows:

$$w_{\text{trpl}} = P_{\text{Rx}}^{(\text{dB})} - \hat{r}_{\text{trpl}}^{(\text{dB})} = Z, \quad (8)$$

where $P_{\text{Rx}}^{(\text{dB})}$ is the measured RSRP sample and Z serves as a simplified notation for the SF variable (equivalent to w in (5)). These known Z values serve as the primary inputs for predicting the SF at unsampled locations by exploiting its spatial correlation properties.

This study introduces a novel algorithm that leverages both Gaussian process regression (GPR) and matrix completion (MC) for shadowing prediction. For performance comparison, we employ ordinary Kriging (OK) [54], simple Kriging (SK) [55], and their respective trans-Gaussian variants [56]. In the following subsections, we provide the formulations for our proposed MC-assisted GPR, which specifically targets improved accuracy in deep-shadowed regions.

A. Ordinary Kriging (OK)

Let the 3D coordinates of the M sparse measurement locations be denoted by $\{l_1, \dots, l_M\}$, where M represents the number of available sparse samples. The corresponding SF components at these locations are denoted by $Z(l_i)$, where $l_i = (\psi_i, \zeta_i, h_i)$ corresponds to the latitude, longitude, and altitude, respectively. OK employs a linear combination of these known measurements to predict the signal $\hat{Z}(l_0)$ at a new location l_0 . Its objective is to minimize the squared estimation error while ensuring that the sum of the weights used for linear combination equals 1. Formally, it can be written as:

$$\begin{aligned} \min_{w_1, \dots, w_M} \mathbb{E} \left[\left(\hat{Z}(l_0) - Z(l_0) \right)^2 \right], \\ \text{s.t. } \hat{Z}(l_0) = \sum_{i=1}^M w_i Z(l_i), \\ \sum_{i=1}^M w_i = 1. \end{aligned} \quad (9)$$

This constrained minimization problem can be solved using the method of Lagrange multipliers, which reduces the opti-

mization to the following system of linear equations:

$$\begin{bmatrix} \gamma(l_1, l_1) & \cdots & \gamma(l_1, l_M) & 1 \\ \vdots & \ddots & \vdots & \vdots \\ \gamma(l_M, l_1) & \cdots & \gamma(l_M, l_M) & 1 \\ 1 & \cdots & 1 & 0 \end{bmatrix} \begin{bmatrix} w_1 \\ \vdots \\ w_M \\ \mu \end{bmatrix} = \begin{bmatrix} \gamma(l_0, l_1) \\ \vdots \\ \gamma(l_0, l_M) \\ 1 \end{bmatrix}, \quad (10)$$

where μ is the Lagrange multiplier, and $\gamma(l_i, l_j)$ denotes the semivariogram [57] between two locations l_i and l_j with respect to Z , defined as:

$$\gamma(l_i, l_j) = \text{Var}(Z(l_i) - Z(l_j)), \quad (11)$$

where $\text{Var}(\cdot)$ denotes the variance operator. For zero-mean shadow fading Z , the semivariogram $\gamma(l_i, l_j)$ is related to spatial correlation $R_z(l_i, l_j)$ by the following expression:

$$\gamma(l_i, l_j) = \sigma_Z^2 [1 - R_z(l_i, l_j)], \quad (12)$$

where σ_Z^2 is the variance of Z . The analytical expression for the mean squared error (MSE) in predicting at l_0 is given by:

$$\sigma_{\text{ok}}^2(l_0) = \sum_{i=1}^M w_i \gamma(l_0, l_i) + \mu. \quad (13)$$

It should be noted that OK is classified as a Best Linear Unbiased Estimator (BLUE), where the unbiasedness is ensured by assuming a locally constant but unknown mean and imposing the constraint that the weighting parameters sum to unity.

B. Simple Kriging (SK)

Given M sparse measurement samples, SK estimates the unknown value at a target location l_0 , $\hat{Z}(l_0)$, through a linear combination of the observed samples $Z(l_1), \dots, Z(l_M)$. Unlike OK, SK does not impose a constraint on the sum of the weighting parameters. A constant mean m_Z is assumed for the process Z , which is typically around zero for SF. The objective of SK is to minimize the MSE at an arbitrary location l_0 , as formulated below:

$$\begin{aligned} \min_{\lambda_1, \dots, \lambda_M} \quad & \mathbb{E} \left[\left(\hat{Z}(l_0) - Z(l_0) \right)^2 \right], \\ \text{s.t.} \quad & \hat{Z}(l_0) = m_Z + \sum_{i=1}^M w_i (Z(l_i) - m_Z). \end{aligned} \quad (14)$$

The optimum weights for SK can be computed by solving the following set of linear equations:

$$\begin{bmatrix} C(l_1, l_1) & \cdots & C(l_1, l_M) \\ \vdots & \ddots & \vdots \\ C(l_M, l_1) & \cdots & C(l_M, l_M) \end{bmatrix} \begin{bmatrix} w_1 \\ \vdots \\ w_M \end{bmatrix} = \begin{bmatrix} C(l_0, l_1) \\ \vdots \\ C(l_0, l_M) \end{bmatrix}, \quad (15)$$

where $C(l_i, l_j)$ represents the spatial covariance of Z between two locations l_i and l_j , and is directly related to the spatial correlation $R_Z(l_i, l_j)$ through the SF variance σ_Z^2 as follows:

$$C(l_i, l_j) = \sigma_Z^2 R_z(l_i, l_j). \quad (16)$$

The prediction MSE for SK is given as follows:

$$\sigma_{\text{sk}}^2(l_0) = \sigma_Z^2 - \sum_{i=1}^M w_i C(l_0, l_i). \quad (17)$$

SK is recognized as the Best Linear Predictor (BLP) and is inherently unbiased due to the assumption of a known, constant mean. Furthermore, if the process Z is Gaussian, SK also serves as the global best predictor among all (linear and nonlinear) estimators.

C. Trans-Gaussian Kriging

In some cases, the shadow fading data Z exhibit a skewed distribution. We know that the Gaussian distribution ensures the optimality of a linear predictor over all possible predictors, including nonlinear ones, in terms of minimizing MSE [56, Chapter 3]. Hence, we can transform Z into U that has a standard normal distribution $\mathcal{N}(0, 1)$. The transformation function $f(\cdot)$ can be obtained as follows [58]:

$$U(l) = \text{CDF}_{\mathcal{N}(0,1)}^{-1} \left(\text{CDF}_Z(Z(l)) \right) \equiv f(Z(l)), \quad (18)$$

where $\text{CDF}(\cdot)$ is the cumulative distribution function of a random variable. Let the mean of U be denoted as m_U and the variance of U as σ_U^2 , the inverse function of $f(\cdot)$ as $\phi(\cdot)$, the OK prediction of U as $\hat{U}_{\text{ok}}(\cdot)$, and the SK prediction of U as $\hat{U}_{\text{sk}}(\cdot)$. Their corresponding MSE, calculated using (13) and (17), are denoted as $\sigma_{\hat{U}_{\text{ok}}}^2(\cdot)$ and $\sigma_{\hat{U}_{\text{sk}}}^2(\cdot)$, respectively, and the Lagrange multiplier in (10) is μ_U .

After predicting variable U at location l_0 , we need to transform it back into the Z domain using $\phi(\cdot)$. Moreover, it turns out that estimation in the Z domain introduces a prediction bias if the second-order derivative of $\phi(\cdot)$ computed at m_U is nonzero. To compensate for this bias, the approximately unbiased solution for OK is given as follows [56]:

$$\hat{Z}_{\text{ok}}(l_0) = \phi(\hat{U}_{\text{ok}}(l_0)) + \phi''(m_U) \left[\sigma_{\hat{U}_{\text{ok}}}^2(l_0) / 2 - \mu_U \right]. \quad (19)$$

The equation above is derived using the second-order delta method. Similarly, for SK, the approximately unbiased solution is provided by [56]:

$$\hat{Z}_{\text{sk}}(l_0) = \phi(\hat{U}_{\text{sk}}(l_0)) + \frac{\phi''(m_U)}{2} \left[\sigma_{\hat{U}_{\text{sk}}}^2(s_0) - \sum_{i=1}^n \lambda_i C(l_0, l_i) \right]. \quad (20)$$

D. Gaussian Process Regression (GPR)

In contrast to SK, which models Z as a direct random process with variance σ_Z^2 , GPR treats Z as the sum of a latent stochastic process Y and an additive measurement noise component δ_m . Specifically, $Z(l) = Y(l) + \delta_m$, where l denotes the measurement location and $\delta_m \sim \mathcal{N}(0, \sigma_{\text{GP}}^2)$ represents Gaussian noise with variance σ_{GP}^2 . The latent process Y is assumed to have a zero mean ($m_Y = 0$), with a spatial covariance governed by $C_Y(l_i, l_j) = \sigma_Y^2 R_Y(l_i, l_j)$, where σ_Y^2 is the signal variance and $R_Y(\cdot)$ is the correlation function. The covariance of the noisy observations Z between two locations l_i and l_j then can be expressed as follows:

$$C_Z(l_i, l_j) = C_Y(l_i, l_j) + \sigma_{\text{GP}}^2 \delta_{ij}, \quad (21)$$

where δ_{ij} is the Kronecker delta, which is equal to 1 if $i = j$ and 0 otherwise. For a zero-mean process, the GPR estimate

$\hat{Z}(l_0)$ at an unobserved location l_0 is given by:

$$\hat{Z}(l_0) = \sum_{i=1}^M w_i Z(l_i). \quad (22)$$

The optimal weights w_i for GPR are computed by solving the following system of linear equations, which incorporates the noise regularization along the diagonal:

$$\begin{bmatrix} C_Y(l_1, l_1) + \sigma_{\text{GP}}^2 & \cdots & C_Y(l_1, l_M) \\ \vdots & \ddots & \vdots \\ C_Y(l_M, l_1) & \cdots & C_Y(l_M, l_M) + \sigma_{\text{GP}}^2 \end{bmatrix} \begin{bmatrix} w_1 \\ \vdots \\ w_M \end{bmatrix} = \begin{bmatrix} C_Y(l_0, l_1) \\ \vdots \\ C_Y(l_0, l_M) \end{bmatrix}. \quad (23)$$

The prediction variance for GPR, which represents the uncertainty of reconstruction at location l_0 , is given as follows:

$$\sigma_{\text{GPR}}^2(l_0) = \sigma_Y^2 + \sigma_{\text{GP}}^2 - \sum_{i=1}^M w_i C_Y(l_0, l_i). \quad (24)$$

While the expressions in (23) and (24) are structurally similar to those of SK, GPR is regularized by the noise variance σ_{GP}^2 , making the reconstruction more robust to noise.

E. MC-Assisted GPR for Deep-Shadow Extraction

The core principle of the proposed MC-assisted GPR framework lies in decomposing the REM into two distinct components: a smooth spatial trend and a deep-shadow component, the latter of which is characterized by localized, high-gradient variations in SF. The MC algorithm is first employed to estimate the underlying smooth trend. Subsequently, the deep-shadow regions are identified and enhanced via a grayscale dilation operation. The methodology is detailed as follows:

1) *Sparse Measurements Into Matrix*: MC is a reconstruction process that takes a partially observed matrix as input and recovers the full matrix as output. Since this method is strictly applicable to grid-structured data, the sparse observations must first be transformed into a matrix representation. To facilitate this, we define a bounded 2D region in the horizontal plane that encapsulates the entire UAV trajectory. This region is then discretized into $5 \text{ m} \times 5 \text{ m}$ square grids, where each grid cell corresponds to a unique entry in the matrix. Given M observation samples of Z (defined by latitudes $D_\psi \in \mathbb{R}^M$, longitudes $D_\zeta \in \mathbb{R}^M$, and shadow fading values $D_Z \in \mathbb{R}^M$), we construct an observation matrix \mathbf{Z} by estimating Z at each grid center using (22), denoted as \mathbf{Z}_{ij} . Concurrently, we form a standard deviation matrix Σ from the uncertainty of each prediction σ_{ij} , calculated as the square root of the variance in (24). This yields a matrix \mathbf{Z} alongside its corresponding trustworthiness indicator matrix Σ . The detailed procedure is outlined in lines 13 through 26 of Algorithm 1.

Algorithm 1 MC-Assisted GPR for Deep-Shadow.

```

1: procedure Main
2:   Input:  $D_Z \in \mathbb{R}^M, D_\psi \in \mathbb{R}^M, D_\zeta \in \mathbb{R}^M, \psi_0 \in \mathbb{R}, \zeta_0 \in \mathbb{R}, T_v \in \mathbb{R}$ 
3:   REM Decomposition:
4:    $\hat{Z}_{\text{mc}}, \mathbf{Z} \leftarrow \text{MatrixCompletion}(D_Z, D_\psi, D_\zeta)$ 
5:    $\hat{Z}_\Delta \leftarrow \mathbf{Z} - \hat{Z}_{\text{mc}}$ 
6:    $\hat{Z}_{\text{ds}} \leftarrow \mathbf{Z}_\Delta \cdot (|\mathbf{Z}_\Delta| > T_v)$ 
7:    $\hat{Z}_{\text{smooth}} \leftarrow \mathbf{Z} - \hat{Z}_{\text{ds}}$ 
8:   Deep-Shadow Enhancement:
9:    $\hat{Z}_{\text{ds}} \leftarrow \text{GrayscaleDilation}(\hat{Z}_{\text{ds}})$ 
10:  Prediction:
11:   $\hat{Z} \leftarrow \text{interp2}(\hat{Z}_{\text{smooth}} + \hat{Z}_{\text{ds}}, \psi_0, \zeta_0, \text{"spline"})$ 
12:  procedure MatrixCompletion
13:    Input:  $D_Z \in \mathbb{R}^M, D_\psi \in \mathbb{R}^M, D_\zeta \in \mathbb{R}^M, \alpha \in \mathbb{R}$ 
14:    Initialization:
15:     $d_{\text{grid}} \leftarrow \text{Constant, equivalent to 5 m}$ 
16:     $G_\psi \leftarrow \min(D_\psi) : d_{\text{grid}} : \max(D_\psi)$ 
17:     $G_\zeta \leftarrow \min(D_\zeta) : d_{\text{grid}} : \max(D_\zeta)$ 
18:     $N_r = \text{count}(G_\psi), N_c = \text{count}(G_\zeta)$ 
19:     $S_i \leftarrow \{1, 2, \dots, N_r\}, S_j \leftarrow \{1, 2, \dots, N_c\}$ 
20:     $\mathbf{Z} \in \mathbb{R}^{N_r \times N_c} \quad \triangleright \text{GPR Prediction}$ 
21:     $\Sigma \in \mathbb{R}^{N_r \times N_c} \quad \triangleright \text{Prediction Variance}$ 
22:    Local interpolation:
23:    for  $i \in S_i$  do
24:      for  $j \in S_j$  do
25:         $z_k, v_k \leftarrow \text{GPR}(D_Z, D_\psi, D_\zeta, G_\psi(i), G_\zeta(j))$ 
26:         $\mathbf{Z}_{ij}, \Sigma_{ij} \leftarrow z_k, v_k$ 
27:    Global matrix completion:
28:     $\mathbf{Z} \leftarrow \text{NuclearNormMin}(\mathbf{Z}, \Sigma, \alpha) \quad \triangleright \text{Algorithm 2}$ 
29:    Output:  $\hat{Z}_{\text{mc}}, \mathbf{Z}$ 

```

2) *Constrained Nuclear Norm Minimization*: To capture the global smooth trend of the REM, we employ constrained nuclear norm minimization. This approach minimizes the nuclear norm as a proxy for the matrix rank, thereby enforcing the smooth spatial transitions typically inherent in large-scale propagation maps [16]. Let the SF observation matrix and its corresponding standard deviation matrix from the previous subsection be denoted as $\mathbf{Z}, \Sigma \in \mathbb{R}^{N_r \times N_c}$, where N_r and N_c represent the number of rows and columns, respectively. The entries of these matrices are \mathbf{Z}_{ij} and σ_{ij} . The refined smooth matrix $\hat{\mathbf{Z}}$ is subsequently recovered by solving the following constrained optimization problem [16]:

$$\begin{aligned} & \min_{\hat{\mathbf{Z}} \in \mathbb{R}^{N_r \times N_c}} \|\hat{\mathbf{Z}}\|_* \\ & \text{subject to } \left| \hat{\mathbf{Z}}_{ij} - \mathbf{Z}_{ij} \right| \leq \alpha \sigma_{ij}, \quad \forall (i, j) \end{aligned} \quad (25)$$

where $\|\cdot\|_*$ denotes the nuclear norm and α is a tuning parameter, detailed in Section VII-A, that regularizes the deviation from the GPR estimates \mathbf{Z} . A large α promotes a lower-rank solution by penalizing the nuclear norm of $\hat{\mathbf{Z}}$, potentially filtering out localized spatial variations. Conversely, as $\alpha \rightarrow 0$, the optimization favors data fidelity, preserving the original GPR values. We solve (25) using an iterative approach, as detailed in Algorithm 2, which employs the

Algorithm 2 Constrained nuclear norm minimization.

```

1: procedure NuclearNormMin
2:   Input:  $\mathbf{Z} \in \mathbb{R}^{N_r \times N_c}$ ,  $\Sigma = (\sigma_{ij}^2) \in \mathbb{R}^{N_r \times N_c}$ ,  $\alpha \in \mathbb{R}$ ,  $T_\lambda \in \mathbb{R}$ 
3:   Initialize:
4:    $\hat{\mathbf{Z}} \leftarrow \mathbf{Z}$ ,  $\lambda \leftarrow \|\mathbf{Z}\|_*$ 
5:    $\lambda_{\min} \leftarrow 0$ ,  $\lambda_{\max} \leftarrow \|\mathbf{Z}\|_*$ ,  $\delta_\lambda \leftarrow \infty$ 
6:    $\Omega = \{(i, j) \in \mathbb{N} \times \mathbb{N} \mid i \leq N_r, j \leq N_c\}$ 
7:   Loop:
8:   while  $\exists(i, j) \in \Omega \mid |\hat{Z}_{ij} - Z_{ij}| \geq \alpha \sigma_{ij}$  or  $\delta_\lambda > T_\lambda$  do
9:      $\lambda_{\text{old}} \leftarrow \lambda$ 
10:     $\lambda \leftarrow (\lambda_{\min} + \lambda_{\max})/2$ 
11:     $\hat{\mathbf{Z}} \leftarrow \text{FindNuclearNormApprox}(\hat{\mathbf{Z}}, \lambda)$  ▷ [59]
12:    if  $\exists(i, j) \in \Omega \mid |\hat{Z}_{ij} - Z_{ij}| \geq \alpha \sigma_{ij}$  then  $\lambda_{\min} \leftarrow \lambda$ 
13:    else  $\lambda_{\max} \leftarrow \lambda$ 
14:     $\delta_\lambda \leftarrow |\lambda - \lambda_{\text{old}}|$ 
15:  Output:  $\hat{\mathbf{Z}}$ 

```

FindNuclearNormApprox(\cdot) function [59] to project the input matrix onto a target nuclear norm.

3) *Deep-Shadow Decomposition and Dilation*: Following the acquisition of the GPR-predicted matrix \mathbf{Z} and its smooth counterpart $\hat{\mathbf{Z}}_{\text{mc}}$ (derived via constrained nuclear norm minimization), we identify regions where the absolute difference between the two exceeds a predefined threshold, T_v . These regions are categorized as deep-shadowed zones. Subsequently, a grayscale dilation operation is applied to the isolated deep-shadow matrix to propagate these extrema to neighboring spatial locations. This dilated component is then recombined with the smooth portion to produce the final REM, effectively ensuring that deep shadowing is accounted for in the surrounding neighborhood. The procedure is outlined in lines 5 through 9 of Algorithm 1.

4) *Prediction*: To predict at an unsampled coordinate (ψ_0, ζ_0, h_0) , defined by its latitude, longitude, and altitude, 2D interpolation is performed across latitude and longitude. This process utilizes the discrete matrix grid centers as reference points and is implemented via the MATLAB `interp2(\cdot)` function. This step corresponds to line 11 of Algorithm 1.

VI. ANTENNA PATTERN CALIBRATION AND ENHANCED PROPAGATION MODELING

This section presents the UAV antenna pattern calibration framework. Section VI-A details the calibration methodology, while Section VI-B provides some examples of empirically obtained radiation patterns and associated technical insights.

A. Methodology of Calibration and Propagation Modeling

The radiation pattern of an antenna is modified when operating in close proximity to a UAV. This modification is deterministic; thus, the auxiliary experiment \mathcal{E}' can be used to model the calibrated UAV-antenna pattern, $G_{\text{uav}}^{(\text{APC})}(\phi_r, \theta_r)$, where θ_r and ϕ_r denote the receive elevation and azimuth angles, respectively. This characterization rests on two key assumptions: (i) the ground station antenna radiation pattern

remains consistent with its isolated measurements, and (ii) dominant multipath components are generated by the UAV body rather than external reflectors.

The first assumption is justified by the typical deployment of GSs in isolated, elevated positions. The second assumption is increasingly valid at higher UAV altitudes, where reflections from remote terrestrial objects are spatially filtered, leaving the UAV chassis as the primary scattering source. Under these conditions, the calibrated antenna pattern is formulated as:

$$G_{\text{uav}}^{(\text{APC})}(\phi_r, \theta_r) = \left(\frac{4\pi}{l_{\text{wave}}} \right)^2 \frac{d_{3\text{D}}^2 \cdot \hat{A}_{\text{uav}}(\phi_r, \theta_r, d_{3\text{D}})}{G_{\text{gs}}(\phi_t, \theta_t)}, \quad (26)$$

where the intermediate term $\hat{A}_{\text{uav}}(\phi_r, \theta_r, d_{3\text{D}})$ is given by:

$$\hat{A}_{\text{uav}}(\phi_r, \theta_r, d_{3\text{D}}) = \sqrt{\frac{P_{\text{Rx}}(\phi_r, \theta_r, d_{3\text{D}})}{P_{\text{Tx}}}}. \quad (27)$$

The full derivation of (26) is provided in Appendix I. In practice, $G_{\text{uav}}^{(\text{APC})}(\phi_r, \theta_r)$ calculation requires sufficient measurement samples at each receive angle; when absent, the model can revert to the antenna's baseline isolated radiation pattern.

To enhance the radio propagation model, we first quantify the discrepancy between the calibrated radiation pattern obtained from \mathcal{E}' , and the initial isolated pattern, as follows:

$$\Delta G_{\text{uav}}^{(\text{dB})}(\phi_r, \theta_r) = G_{\text{uav}}^{(\text{APC})^{(\text{dB})}}(\phi_r, \theta_r) - G_{\text{uav}}^{(\text{dB})}(\phi_r, \theta_r). \quad (28)$$

Next, we revise the received power calculation for the calibrated radiation pattern, as shown below:

$$\hat{r}_{\text{trpl}}^{(\text{APC})^{(\text{dB})}} = P_{\text{Tx}}^{(\text{dB})} - \text{PL}_{\text{trpl}}^{(\text{dB})} + \Delta G_{\text{uav}}^{(\text{dB})}(\phi_r, \theta_r). \quad (29)$$

The above equation enhances the radio propagation model by incorporating a deterministic correction term for antenna gain.

B. Calibrated Patterns: Insights from Experimental Data

Using the measurement data from each of the 15 experiments listed in Table IV as training data \mathcal{E}' , we compute the calibrated radiation pattern of the UAV-mounted antenna. Due to space limitations, we show representative results from two experiments of each dataset in Fig. 7 and Fig. 8.

The calibrated azimuth radiation patterns shown in Fig. 7 provide valuable insights. First, although the antennas in the anechoic chamber appear omnidirectional, this is not the case in field experiments. Second, each data collection environment, such as the one depicted in Fig. 4 (LTE I/Q dataset), results in distinct radiation patterns in Fig. 7(a) and Fig. 7(b). For example, the antenna gain increases at around 90° in both Fig. 7(a) and Fig. 7(b), as indicated by ①. In the AFAR environment (Fig. 5), the antenna pattern shows a blockage around 270° in Fig. 7(c) and Fig. 7(d), as highlighted by ②. Similarly, a unique radiation pattern is observed in the multi-band dataset, as shown in Fig. 7(e) and Fig. 7(f). While Fig. 7(a) and (b) vary altitude, (c) and (d) vary trajectory, and (e) and (f) vary bandwidth, the side-by-side comparison of the azimuth patterns confirms that the effective radiation pattern remains largely unaffected by altitude, bandwidth, or trajectory. However, it does vary with the experimental setup, including the characteristics of the GS, the surrounding

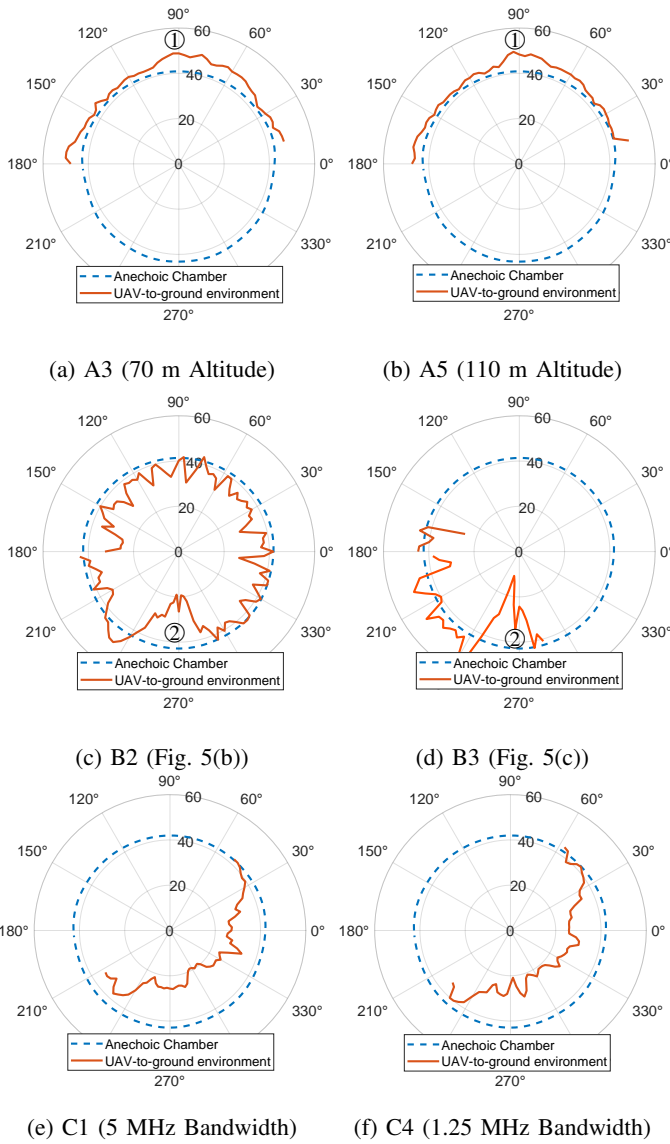


Fig. 7: Azimuth radiation patterns for six experiments from Table IV. The solid line represents the radiation pattern in the experimental environment, while the dashed line represents the radiation pattern in the anechoic chamber. The subfigures are arranged for left-to-right comparison: (a) and (b) compare two *heights*, (c) and (d) compare two *trajectories*, and (e) and (f) compare two *bandwidths*. All other conditions in each row remain identical, except for the one specified in the subcaptions. The plots are based on measurements taken only at low elevation angles (less than 20°).

environment, and the UAV used for sensing. These factors differ across datasets, leading to variations in the radiation patterns across different rows in Fig. 7.

Fig. 8 illustrates the elevation radiation patterns, which, like the azimuth radiation patterns, show similar dependence on the experimental environment, altitude, trajectory, and bandwidth. However, a consistent trend is observed in Fig. 8(a) to Fig. 8(f) across different elevation angles. At lower elevation angles, the radiation pattern based on field measurements shows a significant decrease compared to the anechoic chamber mea-

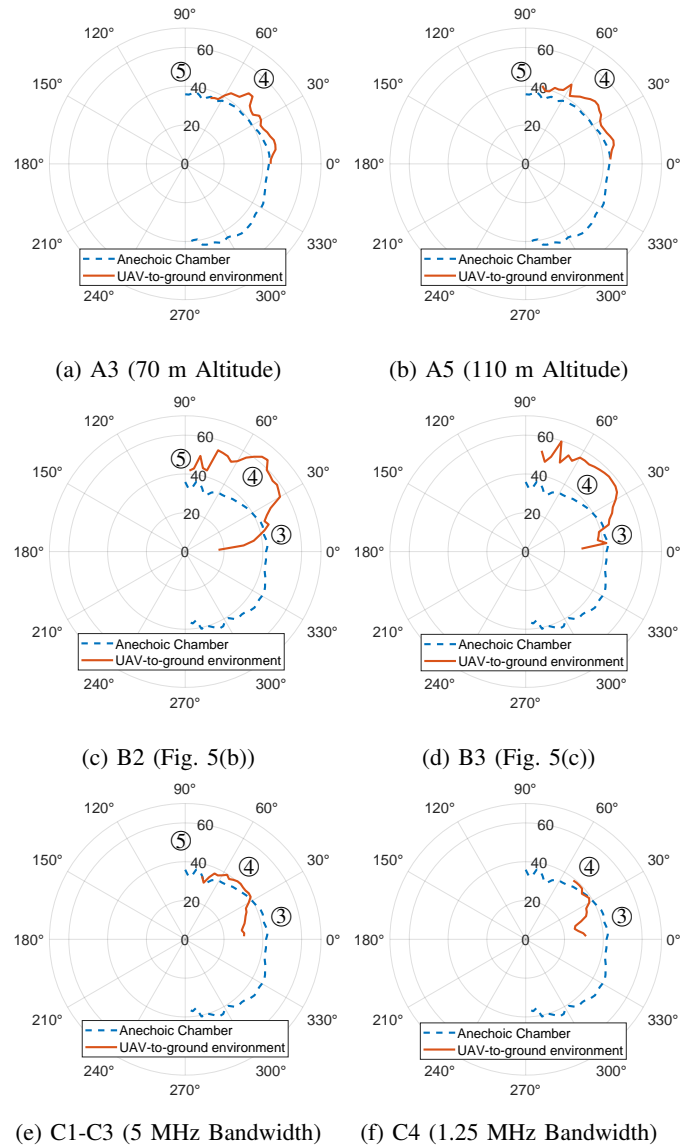


Fig. 8: Elevation radiation patterns for six experiments from Table IV. The solid line represents the radiation pattern in the experimental environment, while the dashed line represents the radiation pattern in the anechoic chamber. The subfigures are arranged for left-to-right comparison: (a) and (b) compare two *heights*, (c) and (d) compare two *trajectories*, and (e) and (f) compare two *bandwidths*. All other conditions of each row remain identical, except for the one specified in the subcaptions. The only exception is (e), which includes experiments from three different altitudes.

surements in Fig. 8(c) to Fig. 8(f), as marked by ③. As the elevation angle increases, the antenna gain surpasses that of the anechoic chamber, as highlighted by ④. At 90° , when the UAV is directly above the ground source, the pattern returns to the anechoic chamber gain, as indicated by ⑤.

The increased antenna gain in Fig. 8(c) and Fig. 8(d), at medium elevation angles, highlighted by ④, is attributed to strong reflections from surfaces near the GS antenna. *The likelihood of reflection is greater in this experimental scenario because the UGV antenna was positioned at a relatively low*

altitude, which enhances the chances of reflections from the UGV surface. In contrast, the BS antenna is expected to interact less with any nearby surfaces. The reduction in gain at lower altitudes, highlighted by ③, is likely due to *increased susceptibility to LoS blocking and/or destructive interference from reflected components* at lower elevation angles. To validate these interpretations, we conducted MATLAB-based ray-tracing simulations, as detailed in Appendix II. By incorporating a 3D UAV object and GS, we reproduced the multipath environments responsible for the observed constructive and destructive interference patterns.

VII. EXPERIMENTAL RESULTS AND ANALYSIS

In this section, we present the experimental results for 3D REM reconstruction. The experimental setup is provided in Section VII-A. The parametric sensitivity of REM reconstruction accuracy across elevation angle, UAV altitude, and spectral bandwidth is evaluated in Sections VII-B through VII-D. Finally, a comparative analysis of REM reconstruction methods, incorporating Kriging variants, antenna pattern calibration, and our proposed MC-assisted GPR, is provided in Sections VII-E through VII-G.

A. Experimental Setup and Evaluation Criteria

1) *Train-Test Split*: As established in Section III-C, the test experiment \mathcal{E} and training experiment \mathcal{E}' are from separate trials. From the target experiment \mathcal{E} , only a limited number of samples M are available for REM reconstruction. To facilitate effective calibration, a distinct training experiment \mathcal{E}' is selected from Table IV based on its proximity to the parameters of \mathcal{E} . Specifically, \mathcal{E}' is chosen as the adjacent experiment with the nearest vertical displacement (e.g., a 20 m altitude separation) or the closest spectral configuration (e.g., a 1.25 MHz bandwidth offset), depending on data availability.

2) *Hyperparameter Settings*: Given M sparse samples, Kriging interpolation utilizes a selection radius R centered at the prediction location, as illustrated in Fig. 9. This localized approach limits the number of active samples, mitigating the potential performance degradation typically associated with high-dimensional Kriging matrices. In this study, R was set to either 70 m or 200 m, where $R = 200$ m was found to fully exploit the spatial interpolation potential of the Kriging framework. The hyperparameters for Algorithm 1 and Algorithm 2 were configured as $\alpha = 1$, $T_v = 1$, and $T_\lambda = 20$.

3) *Evaluation Criteria*: For a given set of M samples, the REM reconstruction accuracy is evaluated using the Root Mean Square Error (RMSE). To ensure statistical significance, the evaluation process was repeated for 5,000 Monte Carlo iterations. In each iteration, M measurement locations were randomly sampled from the test experiment. The median RMSE across these iterations is reported as the primary metric for performance comparison.

B. Sensitivity of REM Accuracy to UAV Elevation Angle

Fig. 10 presents the REM reconstruction performance, in terms of the median RMSE, across elevation angles ranging

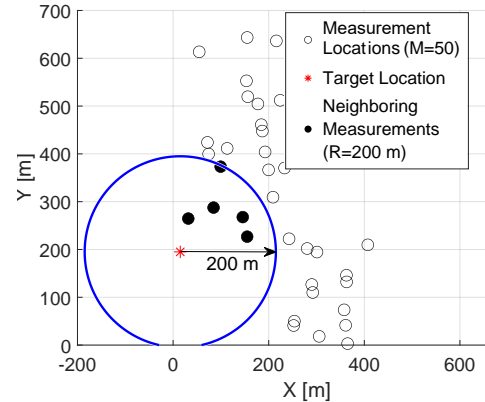


Fig. 9: Illustration of the number of available sparse samples M and sample selection radius R used in Kriging. For predicting at the center of the circle, Kriging utilizes only the samples within the circle.

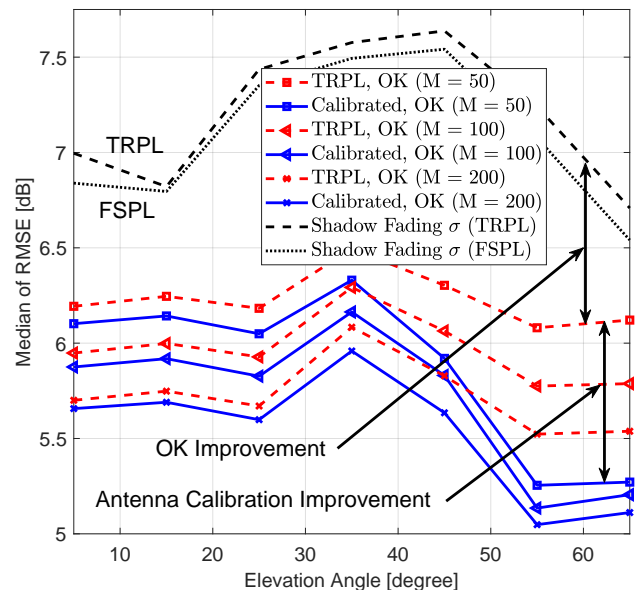


Fig. 10: REM reconstruction accuracy, measured by the median RMSE across elevation angles, comparing the (TRPL, OK) and (Calibrated TRPL, OK) models. The shadowing standard deviation σ , estimated via TRPL and FSPL, is also illustrated. The reduction in RMSE when using (TRPL, OK) relative to the TRPL-estimated σ is identified as the “OK Improvement”, while the further performance gain from the calibrated antenna model is attributed to the calibration.

from 5° to 65° using the LTE I/Q dataset. The reconstruction performance is measured for the deterministic TRPL with OK, and the antenna calibrated TRPL with OK. These results are presented for three sample sizes ($M \in \{50, 100, 200\}$) with $R = 200$ m. The shadowing standard deviation σ , estimated from both TRPL and FSPL, is also plotted as a baseline.

The results indicate that the TRPL-estimated σ varies significantly with elevation: it initially decreases between 5° and 15° , reaches a peak at 45° , and subsequently declines rapidly at steeper elevation angles. Notably, the reconstruction

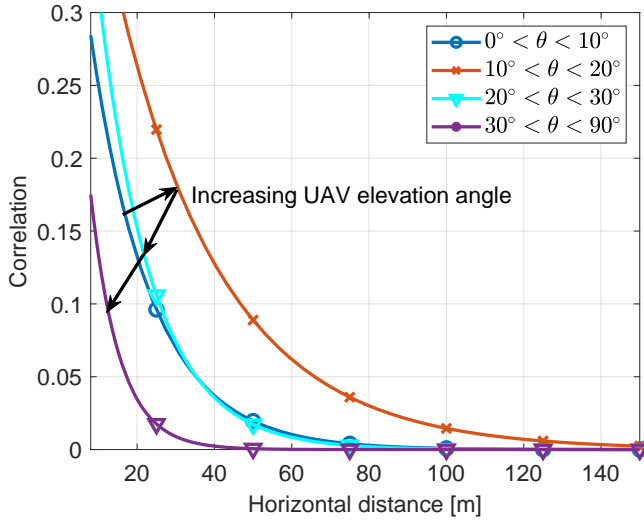


Fig. 11: Shadow fading correlation profile as a function of horizontal distance for varying UAV elevation angles. Correlation strength initially increases with elevation angle, then declines and eventually reaches near-zero correlation.

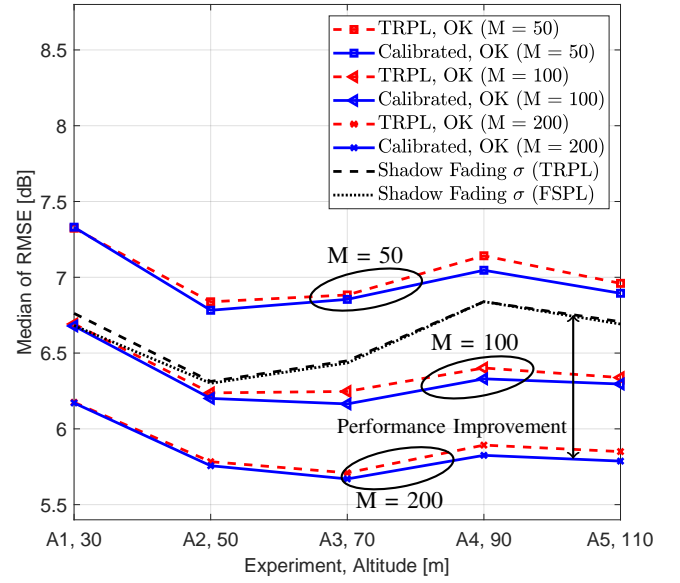
performance of OK (indicated by red dashed lines) does not always align with TRPL-estimated σ . Specifically, at higher elevation angles such as 65° , the performance gain from OK (labeled as “OK improvement”) is comparatively lower.

To investigate the efficacy of OK across elevations, the spatial correlation versus horizontal distance for varying elevation angles is plotted in Fig. 11. The correlation exhibits non-monotonic behavior, increasing up to 20° before declining toward negligible levels at steeper angles. This explains the marginal OK gains observed in Fig. 10 at 65° . It also aligns with the observed trend of lower OK improvement at small elevation angles ($< 10^\circ$), followed by increased gains as the elevation angle increases toward the mid-range.

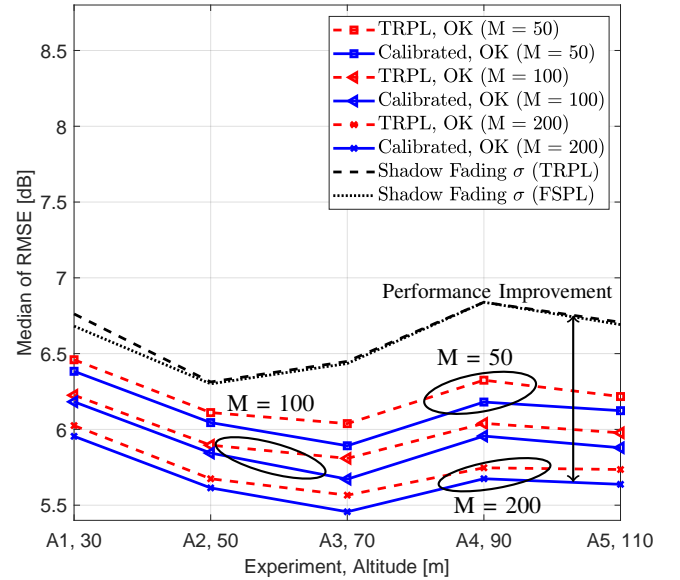
The characteristic profile of the TRPL σ with respect to elevation can be interpreted through the physical propagation environment. At lower elevation angles, the UAV is more susceptible to LoS blockage and a higher density of terrestrial multipath reflections, resulting in higher shadowing variance at 5° compared to 15° . As the elevation angle increases, the UAV clears most terrestrial obstacles, leading to a more LoS-dominant environment and a subsequent reduction in shadowing variance. The shadowing peak centered at 45° is attributed to the ground station’s dipole antenna pattern, which creates localized reception variations in this region. As the elevation increases further, the ground station’s influence diminishes due to the dipole’s radiation nulls, leading to more consistent shadowing behavior in terms of variance.

C. Sensitivity of REM Accuracy to UAV Altitude

Fig. 12 illustrates the median RMSE results for UAV altitudes ranging from 30 m to 110 m, derived from the experimental LTE I/Q dataset. Performance is evaluated for both the baseline TRPL with OK and the antenna-pattern-calibrated TRPL with OK. The estimated shadow fading standard deviation σ is also plotted as a baseline. We observe



(a) $R = 70$ m



(b) $R = 200$ m

Fig. 12: Performance of RSRP prediction across five experiments with increasing altitudes from the LTE I/Q dataset. The results are presented for both TRPL with OK and antenna pattern calibrated TRPL with OK, computed for (a) $R = 70$ m and (b) $R = 200$ m. Reduction of RMSE compared to shadow fading σ is marked as overall “performance improvement”.

that σ exhibits a distinct tri-phasic behavior with respect to altitude: an initial decrease, followed by an increase that peaks at 70 m, and a subsequent decline at higher altitudes. This trend is consistent with the behavior of σ with elevation angle in Fig. 10. The physical interpretation provided in Section VII-B remains applicable here, as altitude and elevation angle are intrinsically linked; the initial decline results from increased LoS dominance, the peak at 90 m is attributed to the ground station’s dipole radiation pattern, and the final decline occurs as the UAV moves into the dipole’s upper nulls.

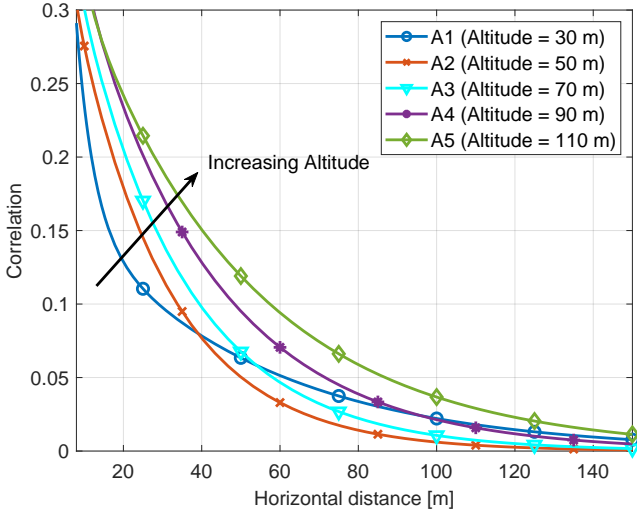


Fig. 13: Correlation profile across horizontal distance for five experiments at increasing altitudes from the LTE I/Q dataset. At higher altitudes, the correlation decays at a slower rate.

The reconstructed REM performance is represented by the red dashed line and the blue solid line (calibrated case). Both models reduce the estimation error below the raw shadowing σ , with the delta identified as the “performance improvement” provided by the OK algorithm. As shown in Fig. 12(b), this improvement increases with altitude. To investigate this altitude-dependent gain, the spatial correlation profiles for discrete altitudes are plotted in Fig. 13. As altitude increases, the spatial correlation decays more slowly, indicating that correlation-based methods like OK are more effective at higher altitudes. This behavior aligns with the elevation-based correlation trends in Fig. 11, as increasing altitude shifts the average elevation angle of the trajectory from the low-elevation regime ($0^\circ < \theta < 10^\circ$) toward the mid-elevation regime ($10^\circ < \theta < 20^\circ$), where spatial correlation is stronger.

Consistent with the tri-phasic behavior of σ , the reconstructed REM performance exhibits a similar tri-phasic trend across altitudes. This behavior is not isolated to this specific dataset; a study by Ivanov *et al.* [20] also demonstrates a similar pattern in their results. Furthermore, we observe this consistent tri-phasic characteristic in results derived from other experimental datasets, as detailed in Appendix III.

Furthermore, Fig. 12(a) shows that with a limited sample size ($M = 50$) and a small selection radius ($R = 70$ m), OK can actually perform worse than simple TRPL-based estimation. However, increasing the selection radius to $R = 200$ m, as shown in Fig. 12(b), significantly enhances the performance, confirming that a larger neighborhood is required for OK for optimal performance under limited sampling, $M \leq 200$.

D. Sensitivity of REM Accuracy to Channel Bandwidth

Fig. 14 presents the median RMSE results for three experiments with bandwidths of 1.25 MHz, 2.5 MHz, and 5 MHz from the multi-band dataset. The altitudes for these datasets were fixed at 40 m, and the horizontal trajectories remained identical across all experiments. The figure plots the perfor-

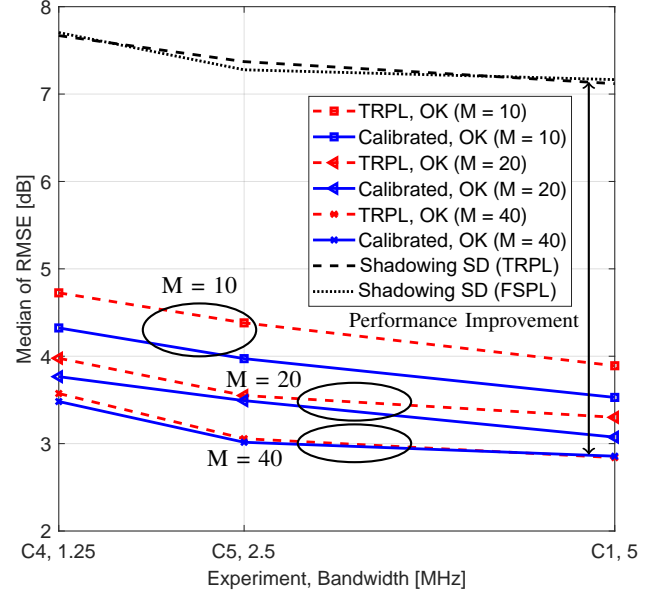


Fig. 14: RSRP prediction error across three experiments with increasing bandwidths from the multi-band dataset.

mance for both TRPL with OK and antenna pattern calibrated TRPL with OK. The observed trend indicates that the prediction error decreases as the bandwidth increases. For instance, the median RMSE is approximately 0.8 dB lower when using TRPL with OK at a 5 MHz bandwidth compared to a 1.25 MHz bandwidth. This behavior is expected, as narrower bandwidths are more susceptible to frequency-selective fading, which increases shadowing variance. For this evaluation, the OK configuration was maintained at $R = 200$ m.

E. Comparative REM Accuracy across Kriging Variants

Fig. 15 illustrates the comparative performance of OK, SK, and their trans-Gaussian variants. The results, shown in Fig. 15(a) and Fig. 15(b), represent the REM reconstruction result using TRPL with a Kriging variant for $R = 70$ m and $R = 200$ m, respectively. In Fig. 15(a), for $R = 70$ m and $M = 50$, SK provides a performance boost of approximately 1 dB, demonstrating the effectiveness of SK when a small number of measurements are used. At $M = 200$, the performance gain of SK diminishes, while trans-Gaussian SK provides the best performance across all altitudes. In Fig. 15(b), SK performs relatively poorly for $R = 200$ m and $M = 200$, indicating that as the number of samples increases, OK becomes a better option. However, trans-Gaussian SK maintains performance at a level comparable to OK. On the other hand, the performance gain from employing trans-Gaussian OK is negligible, with results nearly identical to standard OK.

F. REM Accuracy Enhancement via Antenna Calibration

The impact of antenna pattern calibration on REM reconstruction accuracy was introduced in previous sections, specifically within the contexts of Fig. 12 and Fig. 14. In Fig. 12, the training experiment \mathcal{E}' was characterized by a 20 m vertical displacement from the target experiment \mathcal{E} . Conversely, in

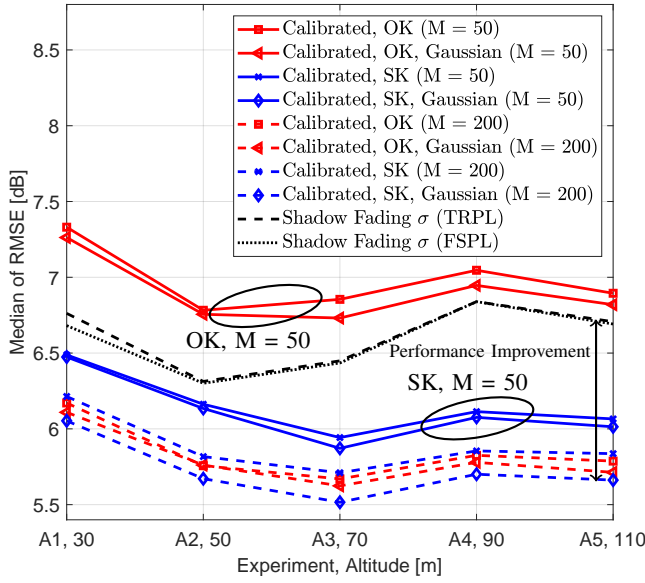
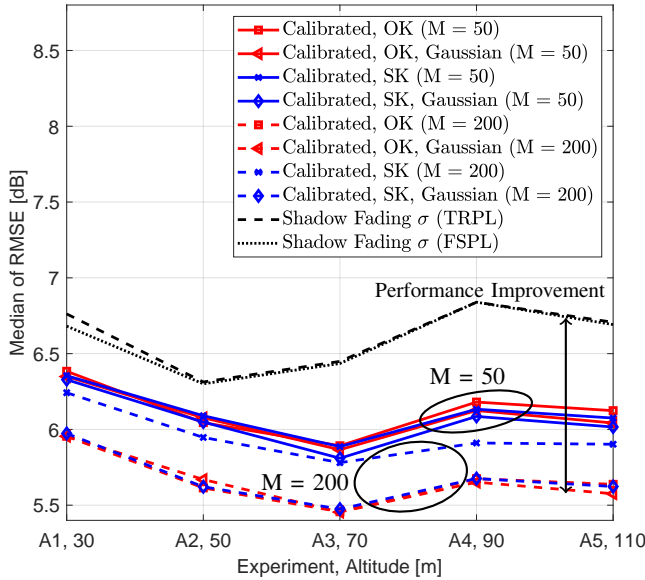

 (a) $R = 70$ m

 (b) $R = 200$ m

Fig. 15: Performance comparison of ordinary Kriging, simple Kriging, and their trans-Gaussian variants across five experiments in LTE I/Q dataset, using calibrated propagation model, computed for (a) $R = 70$ m and (b) $R = 200$ m. Trans-Gaussian simple Kriging shows the best overall performance.

Fig. 14, the separation was defined in the frequency domain, with bandwidth offsets of 1.25 MHz and 2.5 MHz. Fig. 10 demonstrates that the most significant performance variation between the baseline TRPL and the calibrated TRPL occurs at higher elevation angles. This confirms that the error reduction results from the calibrated radiation pattern, which becomes increasingly distinguishable at steeper elevation angles, as illustrated by the calibrated patterns in Fig. 8(a) and Fig. 8(b).

Extending the analysis of altitudinal and spectral separation, we observe that the antenna pattern can also be effectively learned from an experiment \mathcal{E}' employing a distinct horizontal

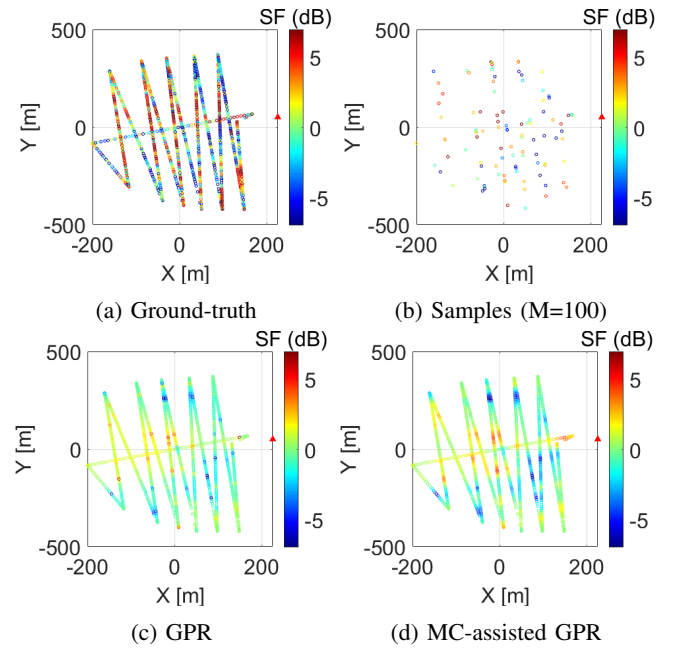


Fig. 16: Shadow Fading (SF) map reconstruction results: (a) ground-truth SF map, (b) observed sparse samples ($M=100$), (c) standard GPR prediction, and (d) MC-assisted GPR prediction. The map in (d) utilizes grayscale dilation to effectively spread deep-shadow regions.

trajectory. The results of this cross-trajectory antenna calibration are provided in Appendix IV. Finally, as discussed in Appendix IV, in scenarios where \mathcal{E}' provides insufficient sampling density for a specific target direction, the framework should revert to the baseline antenna pattern.

G. REM Accuracy Enhancement via MC-Assisted GPR for Deep-shadow Extraction

In this subsection, we evaluate the performance of the proposed MC-Assisted GPR, which is designed to enhance deep-shadowed regions. Using the LTE I/Q experimental dataset, representative SF maps generated by the proposed algorithm and standard GPR are compared in Fig. 16. As illustrated, the standard GPR prediction in Fig. 16(c) tends to treat deep shadow observations (indicated by dark blue or red regions) as isolated singular points. Standard Kriging and GPR algorithms inherently attempt to “erase” or smooth these extrema to minimize global variance, preventing neighboring locations from benefiting from these deep shadow observations. This oversmoothing is counterintuitive in environments where deep shadowing is spatially continuous. In contrast, the proposed MC-assisted GPR specifically identifies these deep-shadowed points and propagates their influence through the local neighborhood using grayscale dilation, as shown in Fig. 16(d).

Fig. 17 presents the REM reconstruction error, measured in median RMSE, for the proposed algorithm compared to OK, SK, and baseline GPR. All algorithms reconstruct the SF maps using TRPL as the deterministic path loss component. The results indicate that GPR generally outperforms OK and SK, as the latter methods require the optimization of the selection radius R for a given sampling density M . At very low sampling

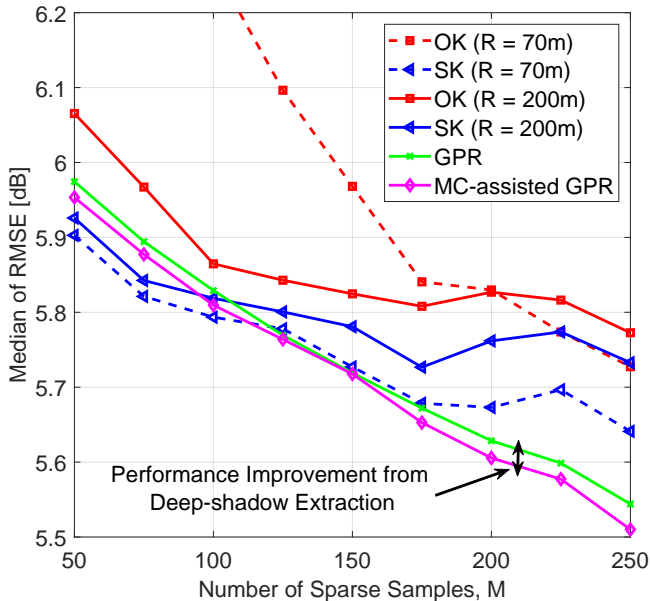


Fig. 17: Comparison of REM reconstruction performance among OK, SK, GPR, and the proposed MC-assisted GPR. In all cases, the standard TRPL serves as the baseline radio propagation model, with the respective algorithms used to reconstruct the shadowing residuals.

densities, SK provides the most accurate results; however, it lacks scalability as M increases, allowing OK to eventually match its performance. GPR, on the other hand, provides reliable and consistent performance gains with increasing M . Because GPR explicitly accounts for measurement noise, it maintains stability even with a high number of observations, unlike SK, which may suffer from matrix ill-conditioning.

Finally, the proposed MC-assisted method consistently enhances GPR performance by effectively characterizing the deep shadow zones. However, this improvement increases computational complexity. Unlike standard GPR, which can perform localized inference at arbitrary points without generating a global map, the MC-assisted approach requires a nuclear norm minimization operation over the full spatial matrix. Furthermore, while GPR operates on continuous spatial coordinates, the matrix-based MC framework necessitates location quantization, meaning the resolution and computational cost are intrinsically linked to the grid density.

VIII. CONCLUSION

This paper presents a comprehensive characterization of 3D REM reconstruction using real-world UAV measurements, providing fundamental insights into the physical and platform-specific drivers of estimation accuracy. We have demonstrated that the impact of UAV altitude on reconstruction fidelity follows a distinct tri-phasic trend, whereas increased spectral bandwidth consistently enhances reconstruction performance. Furthermore, our analysis reveals that shadowing variance is intrinsically linked to elevation angles; lower elevation angles yield higher variance due to reduced LoS dominance, while steep elevation angles experience lower shadowing variance as the UAV transitions into the antenna’s dipole null regions.

From a practical perspective, our findings provide a predictive framework for identifying spatial regions where signal strength is likely to fluctuate rapidly, thereby enabling efficient trajectory planning and spectrum sensing without exclusive reliance on data-intensive deep learning models.

Electromagnetic distortions induced by the UAV airframe cause consistent variations in the radiation pattern that can be empirically captured from measurement data. By utilizing this calibrated pattern, REM reconstruction accuracy is significantly improved. Additionally, we have demonstrated that sparse samples in deep shadowing regions are often filtered or “erased” by standard reconstruction algorithms. By employing GPR with matrix completion, we successfully identified and dilated these shadowed regions, an approach particularly valuable in high-shadowing environments. Ultimately, these insights for single-source scenarios serve as essential building blocks for modeling more complex, multi-source 3D radio environments in future cognitive radio networks.

ACKNOWLEDGMENTS

We use the publicly available field measurement data and the preprocessing scripts [46], [48], [53], [60] published by the NSF Aerial Experimentation and Research Platform on Advanced Wireless (AERPAW) [49], [50] platform. This research is supported in part by the NSF awards CNS-1939334 and CNS-2450593, and the INL Laboratory Directed Research Development (LDRD) Program under BMC No. 264247, Release No. 26 on BEA’s Prime Contract No. DE-AC07-05ID14517.

APPENDIX I

ANALYTICAL DERIVATION OF THE UAV-ANTENNA PATTERN CALIBRATION EQUATION

The received power at a UAV-mounted antenna is the superposition of S discrete multipath components. In a standard two-ray ground reflection model, $S = 2$, comprising the LoS and the ground-reflected ray. However, for an antenna integrated onto a UAV chassis, S is typically larger due to near-field reflections and diffractions from the UAV’s structural components. The total received power is expressed as:

$$P_{Rx}(\phi_r, \theta_r, d_{3D}) = P_{Tx} \left| \sum_{i=1}^S A_i \exp(j\tau_i) \right|^2, \quad (30)$$

where P_{Tx} and P_{Rx} represent the transmitted and received powers in watts, respectively; $(\phi_r, \theta_r, d_{3D})$ denote the receive

Mushfiqur Rahman, İsmail Güvenç, Chau-Wai Wong, and Mihail Sichitiu are with the Department of Electrical and Computer Engineering, North Carolina State University, Raleigh, NC 27606, USA (e-mail: mrahman7@ncsu.edu; iguvenç@ncsu.edu; chauwai.wong@ncsu.edu; mlsichit@ncsu.edu).

Sung Joon Maeng was previously with the Department of Electrical and Computer Engineering, North Carolina State University. He is now with the Department of Electrical and Electronic Engineering, Hanyang University, Ansan 15588, South Korea (e-mail: sjmaeng@hanyang.ac.kr).

Jason A. Abrahamson and Arupjyoti Bhuyan are with the Idaho National Laboratory, Idaho Falls, ID 83402, USA (e-mail: jason.abrahamson@inl.gov; arupjyoti.bhuyan@inl.gov).

azimuth, elevation, and 3D Euclidean distance relative to the GS, as illustrated in Fig. 1. Here, A_i denotes the amplitude attenuation and τ_i represents the phase shift of the i -th ray.

The effective radiation pattern of the UAV-mounted antenna is a composite of the direct LoS ray ($i = 1$) and all secondary rays that interact exclusively with the UAV body along the propagation path. To isolate these platform-specific effects from terrestrial multipath, we exclude the ground-reflected ray ($i = 2$) and define a resultant ‘‘UAV-effective’’ phasor, $A_{\text{uav}} \exp(j\tau_{\text{uav}})$, as follows:

$$A_{\text{uav}} \exp(j\tau_{\text{uav}}) = \sum_{\substack{i=1 \\ i \neq 2}}^S A_i \exp(j\tau_i). \quad (31)$$

This resultant phasor accounts for all scattering and diffraction contributions intrinsic to the UAV platform. Consequently, (30) can be simplified as follows:

$$P_{\text{Rx}}(\phi_r, \theta_r, d_{3\text{D}}) = P_{\text{Tx}} \left| \sum_{i \in \{\text{uav}, 2\}} A_i \exp(j\tau_i) \right|^2. \quad (32)$$

To obtain the radiation pattern of the UAV-mounted antenna, A_{uav} , a practical estimation method is required. While anechoic chamber measurements provide high precision, they are cost-prohibitive and must be repeated for every structural customization of the UAV body. In-field estimation via (32) serves as a viable alternative. However, solving for A_{uav} remains challenging because P_{Rx} represents power (magnitude squared), whereas the constituent components are complex phasors. A full reconstruction would typically require channel-sounding waveforms to resolve individual phase contributions. Furthermore, at a carrier frequency of 3.5 GHz, the wavelength ($\lambda \approx 8.6$ cm) makes the phase of the reflected ray highly sensitive to small variations in the environment. Given that natural grasslands are not perfectly planar and that slight inaccuracies in 3D distance measurements are inevitable, the deterministic calculation of the reflected ray’s phase is often unreliable. However, since the reflectivity of vegetation is significantly lower than that of the metallic components typical of UAV chassis, the impact of the ground-reflected ray can be considered secondary in high-altitude scenarios. By neglecting the ground-reflected component, we can approximate the UAV-effective term from (32) as:

$$\hat{A}_{\text{uav}}(\phi_r, \theta_r, d_{3\text{D}}) \approx \sqrt{\frac{P_{\text{Rx}}(\phi_r, \theta_r, d_{3\text{D}})}{P_{\text{Tx}}}}. \quad (33)$$

The resulting \hat{A}_{uav} in (33) represents the total path gain, which inherently contains the spatial characteristics of the UAV-mounted antenna. To isolate the UAV-antenna radiation pattern, $G_{\text{uav}}^{(\text{APC})}(\phi_r, \theta_r)$, we normalize this quantity by accounting for the 3D free-space path loss and the GS antenna gain:

$$G_{\text{uav}}^{(\text{APC})}(\phi_r, \theta_r) = \left(\frac{4\pi}{l_{\text{wave}}} \right)^2 \frac{d_{3\text{D}}^2 \cdot \hat{A}_{\text{uav}}(\phi_r, \theta_r, d_{3\text{D}})}{G_{\text{gs}}(\phi_t, \theta_t)}, \quad (34)$$

where l_{wave} is the wavelength, $G_{\text{gs}}(\phi_t, \theta_t)$ denotes the gain of the GS antenna at the departure angles (ϕ_t, θ_t) , and $d_{3\text{D}}$ is the 3D Euclidean distance.

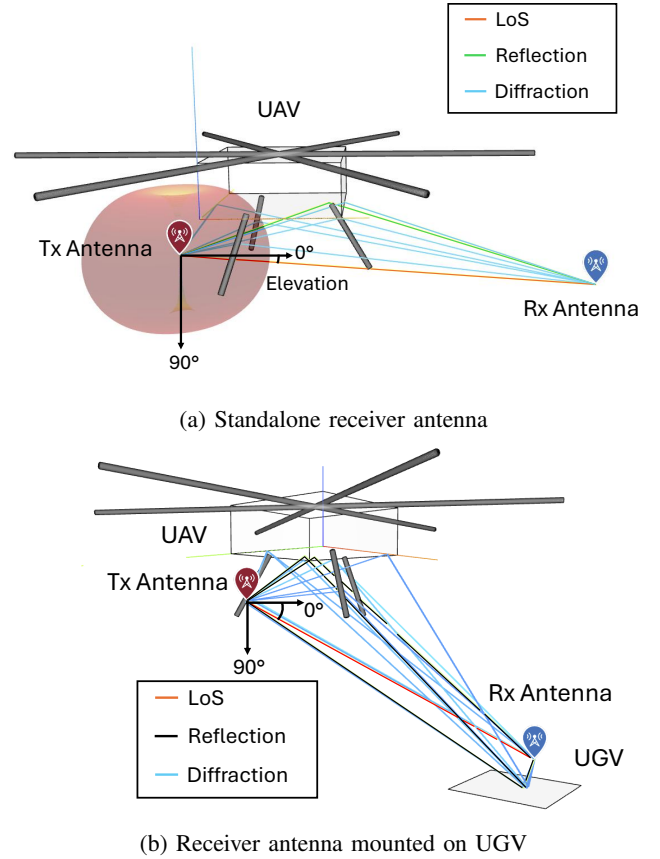


Fig. 18: MATLAB ray tracing simulation environment for measuring the effective radiation pattern of a UAV antenna: (a) with a standalone receiver antenna, (b) with a receiver antenna mounted on a UGV.

APPENDIX II SIMULATED RADIATION PATTERN OF UAV-ANTENNA

To validate our hypotheses regarding ④ and ③ observed in Fig. 8 (i.e., at medium and lower elevation angles, respectively), we conduct a ray tracing simulation using MATLAB. In a 3D environment, we model a UAV with six propeller arms, three landing gears, and a metal cuboid measuring 50 cm by 50 cm by 20 cm, as shown in Fig. 18(a). The UAV antenna, oriented downward, is positioned 20 cm below the UAV’s center and 40 cm to the left, providing a lateral offset. This positioning is suitable for reflecting rays in the opposite horizontal direction, utilizing the bottom surface of the cuboid. The design is inspired by the UAV-based spectrum sensor, where the cuboid represents the portable node attached beneath the UAV. To measure the radiation pattern of the UAV-mounted antenna, an isotropic receiver antenna is positioned at approximately 500 m from the UAV, with elevation angles ranging from 0° to 90° relative to the UAV antenna. Additionally, we repeated the simulation with an extra metallic surface measuring 100 cm by 100 cm, placed 12 cm beneath the receiver antenna, as shown in Fig. 18(b). The azimuth angle range spans 20°, centered on the direction where reflections from the UAV and UGV surfaces are most prominent. For ray tracing, the maximum number of reflections and diffractions was set to 2 and 1, respectively.

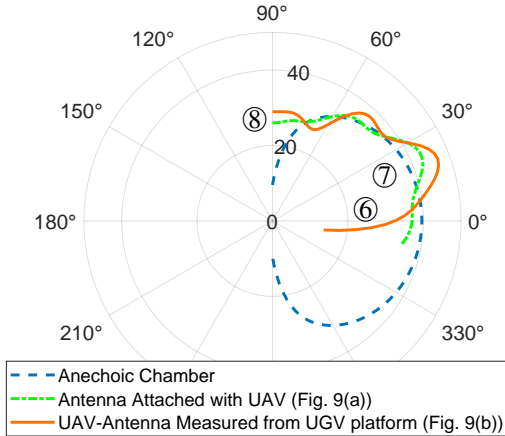


Fig. 19: The elevation radiation pattern of a UAV-mounted antenna, which initially exhibits a dipole pattern when measured standalone in an anechoic chamber. The effective radiation pattern of the UAV-mounted antenna is computed using (33) and (34) within a MATLAB simulation environment, as shown in Fig. 18(a) and Fig. 18(b).

The pattern of received power strength at various elevation angles is illustrated in Fig. 19. At lower elevation angles, highlighted by ⑥, the measurement environments of both Fig. 18(a) and Fig. 18(b) show reduced antenna gain. Further analysis reveals that the lower gain in Fig. 18(a) is primarily due to destructive interference of the reflected ray, while in Fig. 18(b), the gain is further diminished by LoS blocking. At medium elevation angles, highlighted by ⑦, the effective antenna gain increases due to constructive interference of the reflected rays. In Fig. 18(b), the number of reflected rays increases, leading to an even greater gain. Because of the limited size of the UAV cuboid, the reflected rays from the UAV disappear beyond 30° elevation, and the effective pattern in Fig. 18(a) begins to resemble the anechoic chamber patterns after 30° . In contrast, the size and placement of the additional UGV surface in Fig. 18(b) continue to generate reflected rays at higher elevation angles, leading to periodic constructive and destructive interference as the elevation angle increases. Finally, at around the 90° elevation angle, the effective antenna gain is significantly higher than that of the anechoic chamber. This is because the diffracted rays reach the 90° elevation angle, becoming stronger than the LoS ray. For a dipole pattern, the antenna gain at 90° elevation angle is extremely low, so the diffracted rays dominate.

APPENDIX III

TRI-PHASIC REM ACCURACY ACROSS ALTITUDES: TWO ADDITIONAL CASE STUDIES

A. Multi-band dataset

Fig. 20 presents the results of the median of RMSE for three experiments from the multi-band dataset, with altitudes 40 m, 70 m, and 100 m. As observed, the estimated shadow fading standard deviation σ is highest at the intermediate altitude of 70 m. Given that this dataset only includes three altitude samples, it serves as a partial observation of the previously

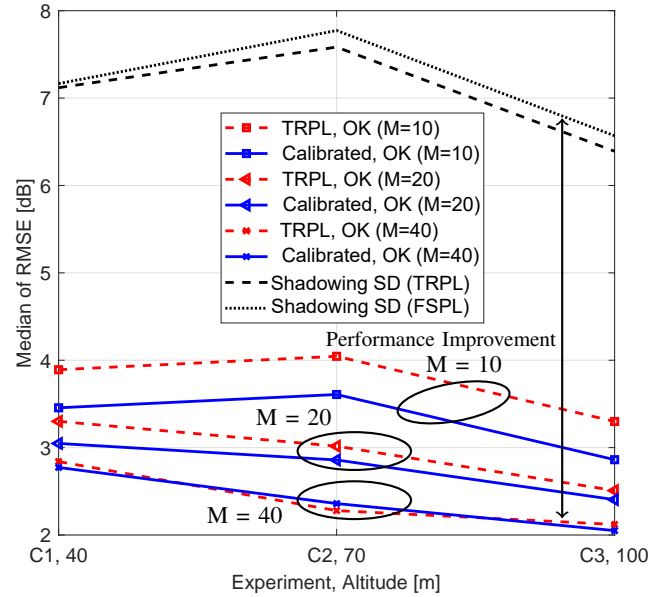


Fig. 20: Performance of RSRP prediction across three experiments with increasing altitudes from the Multi-band dataset. The results are presented for both TRPL with OK and antenna pattern calibrated TRPL with OK.

identified tri-phasic behavior of σ . If additional measurements were available at altitudes closer to the ground, we would expect a higher σ compared to the 40 m case, driven by the increased presence of ground-level multipath reflections and clutter. Thus, the current three-point profile likely captures the mid-altitude peak and the subsequent transition toward the high-altitude LoS-dominant regime. The reconstruction error curves using OK also follow the trend of σ .

B. AFAR dataset

Fig. 21 presents the median RMSE results for TRPL with OK and SK. Fig. 21 presents the median RMSE results using TRPL with OK and SK for the experimental AFAR dataset. The experiments are arranged in ascending order of UAV altitudes, ranging from 21 m to 47 m. Notably, in this dataset, the GS was a UGV with an antenna height of approximately 1.5 m. The estimated shadow fading standard deviation σ across these experiments exhibits a tri-phasic behavior: σ initially decreases from 21 m to 28 m, increases at 37 m, and subsequently declines at 47 m. While these experiments utilized distinct 2D trajectories (as illustrated in Fig. 5), the significant fluctuations in σ are predominantly attributed to the variations in UAV altitude rather than the specific horizontal paths. Interestingly, the reconstructed REM error trends do not strictly mirror the σ profile, particularly at the 37 m and 47 m altitudes. This divergence occurs because higher altitudes result in stronger spatial correlation; consequently, the performance gains provided by OK and SK are more pronounced at these heights, decoupling the reconstruction error trend from the underlying environmental variance σ .

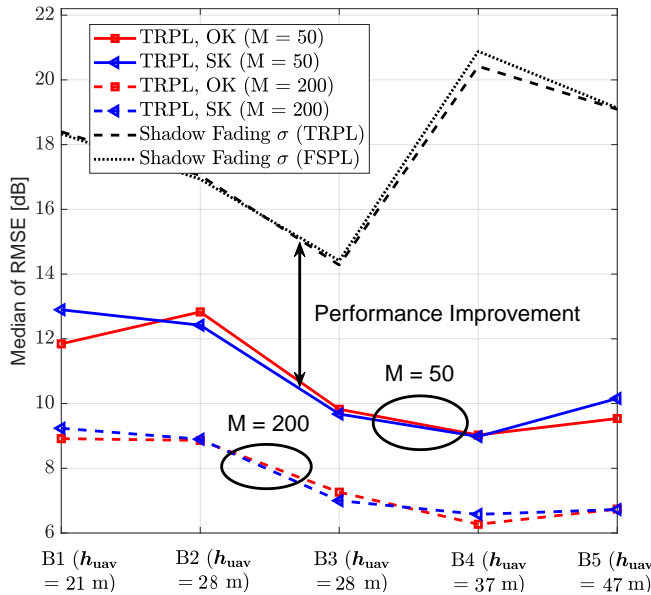


Fig. 21: Performance of RSRP prediction across five experiments with non-decreasing altitudes from the AFAR dataset. The results are presented for TRPL with OK and SK.

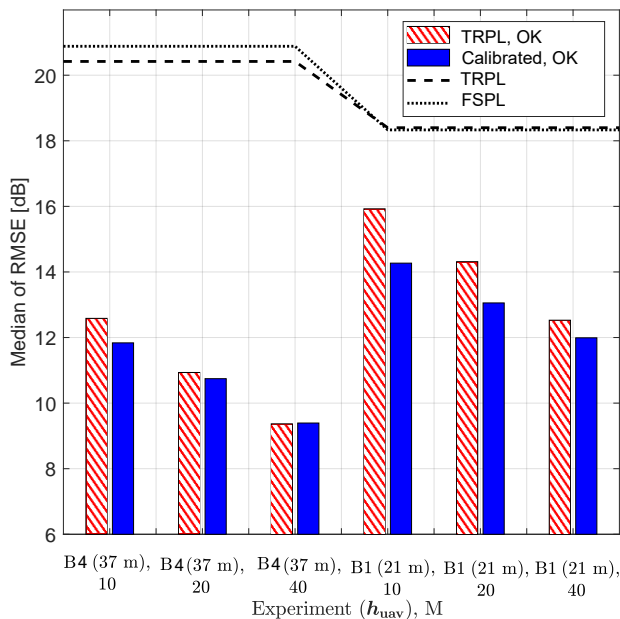


Fig. 22: Comparison of the performance of the TRPL and calibrated TRPL across two experiments from the AFAR dataset. The calibrated model shows improved performance at lower sampling rate, M .

APPENDIX IV INTER-TRAJECTORY ANTENNA CALIBRATION

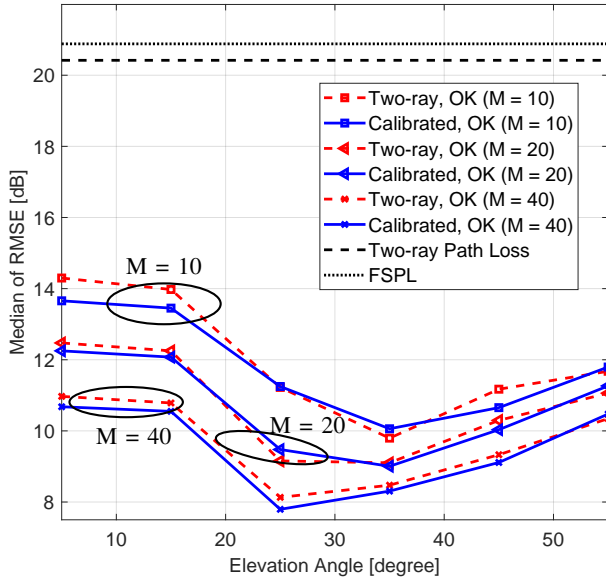
Fig. 22 presents the REM reconstruction performance of the antenna calibrated TRPL compared to the baseline TRPL using the AFAR dataset. The AFAR dataset comprises five experiments of varied trajectories as shown in Fig. 5. Calibrating the antenna pattern using data from a different trajectory seems

more challenging than calibrating from a different altitude of the same trajectory. This is because changing the altitude of the same trajectory only affects the elevation angle of signal reception, while varying the trajectory also alters the azimuth angle. Therefore, we carefully select experiments for antenna pattern calibration. Specifically, experiment B5 is used for calibration when testing on experiment B4, due to the similarity between their trajectories. Similarly, we calibrate the effective antenna pattern using data from experiments B2 and B3 to test on experiment B1. The results of REM reconstruction with the calibrated pattern for experiments B4 and B1 are shown in Fig. 22. The results show that the effective radiation pattern is more helpful when the number of measurements M is smaller, similar to previous cases. The maximum improvement, approximately 2 dB, is observed for experiment B1 with $M = 10$.

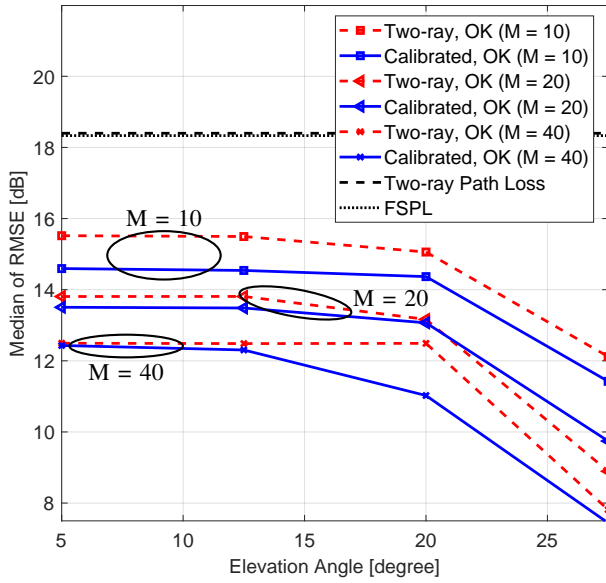
To further investigate the cases, we plot the median RMSE across elevation angles for experiments B4 and B1 in Fig. 23. The comparative plots for the TRPL and calibrated TRPL suggest that the error is reduced for lower elevation angles (less than 20°) in both cases, which corresponds to learning the deep fades at these elevation angles, as demonstrated in Fig. 8(c) and Fig. 8(d). While experiment B1 in Fig. 23(b) does not have samples above 30° , the results from experiment B4 in Fig. 23(a) indicate that the performance of the calibrated model, is degraded for larger elevation angles compared to the TRPL. This suggests that the radiation pattern is not adjusted for higher elevation angles. This is due to the lack of samples in experiment B5 to properly learn the effective radiation pattern for the specific azimuth and elevation angles visited by experiment B4. In such scenarios, the system may revert to the baseline radiation pattern as a default model when the sampling density is insufficient in the target direction.

REFERENCES

- [1] J. Wang, Q. Zhu, Z. Lin, Q. Wu, Y. Huang, X. Cai, W. Zhong, and Y. Zhao, "Sparse Bayesian learning-based 3-D radio environment map construction—sampling optimization, scenario-dependent dictionary construction, and sparse recovery," *IEEE Trans. Cognitive Commun. Netw.*, vol. 10, no. 1, pp. 80–93, 2023.
- [2] F. Zhou, C. Wang, G. Wu, Y. Wu, Q. Wu, and N. Al-Dhahir, "Accurate spectrum map construction for spectrum management through intelligent frequency-spatial reasoning," *IEEE Trans. Commun.*, vol. 71, no. 7, pp. 3932–3945, 2023.
- [3] X. Du, Q. Zhu, G. Ding, J. Li, Q. Wu, T. Lan, Z. Lin, W. Zhong, and L. Han, "UAV-assisted three-dimensional spectrum mapping driven by spectrum data and channel model," *Symmetry*, vol. 13, no. 12, p. 2308, 2021.
- [4] F. Shen, G. Ding, Z. Wang, and Q. Wu, "UAV-based 3D spectrum sensing in spectrum-heterogeneous networks," *IEEE Trans. Vehi. Technol.*, vol. 68, no. 6, pp. 5711–5722, 2019.
- [5] Z. Wei, R. Yao, J. Kang, X. Chen, and H. Wu, "Three-dimensional spectrum occupancy measurement using UAV: Performance analysis and algorithm design," *IEEE Sensors J.*, vol. 22, no. 9, pp. 9146–9157, 2022.
- [6] D. Romero, R. Shrestha, Y. Teganya, and S. P. Chepuri, "Aerial spectrum surveying: Radio map estimation with autonomous UAVs," in *Proc. IEEE Int. Workshop Machine Learning Signal Process. (MLSP)*, September 2020, pp. 1–6.
- [7] R. Shrestha, D. Romero, and S. P. Chepuri, "Spectrum surveying: Active radio map estimation with autonomous UAVs," *IEEE Trans. Wireless Commun.*, vol. 22, no. 1, pp. 627–641, 2022.
- [8] A. Ivanov, B. Muhammad, K. Tonchev, A. Mihovska, and V. Poulkov, "UAV-based volumetric measurements toward radio environment map construction and analysis," *Sensors*, vol. 22, no. 24, p. 9705, 2022.



(a) Experiment B4



(b) Experiment B1

Fig. 23: REM reconstruction error across elevation angles using TRPL and calibrated TRPL for (a) experiment B4 and (b) experiment B1. The calibrated model shows improvement for elevation angles up to 20° . The results are obtained using OK with $R = 70$ m.

[9] Q. Zhu, Y. Zhao, Y. Huang, Z. Lin, L. H. Wang, Y. Bai, T. Lan, F. Zhou, and Q. Wu, "Demo abstract: An UAV-based 3D spectrum real-time mapping system," in *Proc. IEEE Conf. Computer Commun. Workshops (INFOCOM WKSHPS)*, May 2022, pp. 1–2.

[10] P. Zeng and J. Chen, "UAV-aided joint radio map and 3D environment reconstruction using deep learning approaches," in *Proc. IEEE Int. Conf. Commun.*, Seoul, South Korea, May 2022, pp. 5341–5346.

[11] M. Pesko, T. Javornik, L. Vidmar, A. Košir, M. Štular, and M. Mohorčič, "The indirect self-tuning method for constructing radio environment map using omnidirectional or directional transmitter antenna," *EURASIP J. Wireless Commun. Netw.*, vol. 2015, pp. 1–12, 2015.

[12] E. Krijestorac, S. Hanna, and D. Cabric, "Spatial signal strength prediction using 3D maps and deep learning," in *Proc. IEEE Int. Conf.*

Commun. IEEE, June 2021, pp. 1–6.

[13] R. Levie, Ç. Yapar, G. Kutyniok, and G. Caire, "RadioUNet: Fast radio map estimation with convolutional neural networks," *IEEE Trans. Wireless Commun.*, vol. 20, no. 6, pp. 4001–4015, 2021.

[14] Y. Teganya and D. Romero, "Deep completion autoencoders for radio map estimation," *IEEE Trans. Wireless Commun.*, vol. 21, no. 3, pp. 1710–1724, 2021.

[15] K. Mao, Q. Zhu, M. Song, H. Li, B. Ning, G. F. Pedersen, and W. Fan, "Machine-learning-based 3-D channel modeling for U2V mmWave communications," *IEEE Internet of Things Journal*, vol. 9, no. 18, pp. 17 592–17 607, 2022.

[16] H. Sun and J. Chen, "Propagation map reconstruction via interpolation assisted matrix completion," *IEEE Trans. Sig. Process.*, vol. 70, pp. 6154–6169, 2022.

[17] W. Liu and J. Chen, "UAV-aided radio map construction exploiting environment semantics," *IEEE Trans. Wireless Commun.*, vol. 22, no. 9, pp. 6341–6355, 2023.

[18] S. J. Maeng, O. Ozdemir, İ. Güvenç, and M. L. Sichertiu, "Kriging-Based 3-D Spectrum Awareness for Radio Dynamic Zones Using Aerial Spectrum Sensors," *IEEE Sensors J.*, vol. 24, no. 6, pp. 9044–9058, 2024.

[19] T. Hu, Y. Huang, J. Chen, Q. Wu, and Z. Gong, "3D radio map reconstruction based on generative adversarial networks under constrained aircraft trajectories," *IEEE Trans. Vehi. Technol.*, vol. 72, no. 6, pp. 8250–8255, 2023.

[20] A. Ivanov, K. Tonchev, V. Poulkov, A. Manolova, and A. Vlahov, "Limited sampling spatial interpolation evaluation for 3D radio environment mapping," *Sensors*, vol. 23, no. 22, p. 9110, 2023.

[21] W. Locke, N. Lokhmachev, Y. Huang, and X. Li, "Radio map estimation with deep dual path autoencoders and skip connection learning," in *Proc. IEEE Annual Int. Symp. Personal, Indoor, Mobile Radio Commun. (PIMRC)*, Toronto, Canada, September 2023, pp. 1–6.

[22] S. Zhang, A. Wijesinghe, and Z. Ding, "RME-GAN: A learning framework for radio map estimation based on conditional generative adversarial network," *IEEE Internet of Things J.*, vol. 10, no. 20, pp. 18 016–18 027, 2023.

[23] A. Chaves-Villota and C. A. Viteri-Mera, "DeepREM: Deep-learning-based radio environment map estimation from sparse measurements," *IEEE Access*, vol. 11, pp. 48 697–48 714, 2023.

[24] J. Wang, Q. Zhu, Z. Lin, J. Chen, G. Ding, Q. Wu, G. Gu, and Q. Gao, "Sparse Bayesian learning-based hierarchical construction for 3D radio environment maps incorporating channel shadowing," *IEEE Trans. Wireless Commun.*, vol. 23, no. 10, pp. 14 560–14 574, 2024.

[25] M. Rahman, S. J. Maeng, İ. Güvenç, and C.-W. Wong, "3D Spectrum Awareness for Radio Dynamic Zones Using Kriging and Matrix Completion," in *Proc. IEEE Int. Symp. Dynamic Spectrum Access Netw. (DySPAN)*, Washington, DC, USA, May 2024, pp. 439–446.

[26] X. Wang, K. Tao, N. Cheng, Z. Yin, Z. Li, Y. Zhang, and X. Shen, "RadioDiff: An effective generative diffusion model for sampling-free dynamic radio map construction," *IEEE Trans. Cognitive Commun. Netw.*, vol. 11, no. 2, pp. 738–750, 2024.

[27] H. A. Alobaidy, M. Behjati, R. Nordin, M. A. Zulkifley, N. F. Abdullah, and N. F. M. Salleh, "Empirical 3-D channel modeling for cellular-connected UAVs: A triple-layer machine learning approach," *IEEE Open J. Commun. Societ.*, vol. 6, pp. 9908–9925, 2025.

[28] P. Gajewski, "Propagation models in radio environment map design," in *Proc. IEEE Baltic URSI Symposium (URSI)*, Poznan, Poland, May 2018, pp. 234–237.

[29] K. Sato and T. Fujii, "Kriging-based interference power constraint: Integrated design of the radio environment map and transmission power," *IEEE Trans. Cognitive Commun. Netw.*, vol. 3, no. 1, pp. 13–25, 2017.

[30] A. Ivanov, A. Vlahov, V. Poulkov, T. Yioultis, and Z. Zaharis, "Calibration of Statistical Interpolation through Anechoic Chamber Measurements for 3D REM Reconstruction," in *Proc. Int. Symp. Wireless Personal Multimedia Commun. (WPMC)*, India, November 2024, pp. 1–5.

[31] T. Farnham, "Radio environment map techniques and performance in the presence of errors," in *Proc. IEEE Annual Int. Symp. Personal, Indoor, Mobile Radio Commun. (PIMRC)*, Valencia, Spain, September 2016, pp. 1–6.

[32] H. Xia, S. Zha, J. Huang, and J. Liu, "Radio environment map construction by adaptive ordinary Kriging algorithm based on affinity propagation clustering," *Int. J. Distributed Sensor netw.*, vol. 16, no. 5, p. 1550147720922484, 2020.

[33] A. Ivanov, K. Tonchev, V. Poulkov, and A. Manolova, "Deep learning for reduced sampling spatial 3D REM reconstruction," *IEEE Open J. Commun. Societ.*, 2024.

- [34] G. Reddy, I. Guvenc, M. L. Sichitiu, A. Bhuyan, B. Petersen, and J. Abrahamson, "TransfoREM: Transformer aided 3D radio environment mapping," *arXiv preprint arXiv:2601.16421*, 2026.
- [35] S. Zhang, S. Jiang, W. Lin, Z. Fang, K. Liu, H. Zhang, and K. Chen, "Generative AI on SpectrumNet: An open benchmark of multiband 3-D radio maps," *IEEE Trans. Cognitive Commun. Netw.*, vol. 11, no. 2, pp. 886–901, 2024.
- [36] G. Zhang, X. Fu, J. Wang, X.-L. Zhao, and M. Hong, "Spectrum cartography via coupled block-term tensor decomposition," *IEEE Trans. Sig. Process.*, vol. 68, pp. 3660–3675, 2020.
- [37] L. Wang, J. Hu, D. Jiang, and Z. Chen, "A robust learning framework for spatial-temporal-spectral radio map prediction," *Expert Syst. Appl.*, p. 129351, 2025.
- [38] S. Masrur and I. Güvenç, "Bridging simulation and reality: A 3D clustering-based deep learning model for UAV-based RF source localization," in *Proc. IEEE Int. Conf. Commun. Workshops (ICC Workshops)*, Montreal, Canada, June 2025, pp. 953–958.
- [39] F. Shen, Z. Wang, G. Ding, K. Li, and Q. Wu, "3D compressed spectrum mapping with sampling locations optimization in spectrum-heterogeneous environment," *IEEE Trans. Wireless Commun.*, vol. 21, no. 1, pp. 326–338, 2021.
- [40] K. Tsukamoto, M. Kitsunezuka, and K. Kunihiro, "Highly accurate radio environment mapping method based on transmitter localization and spatial interpolation in urban LoS/NLoS scenario," in *Proc. IEEE Topical Conf. Wireless Sensors Sensor Netw. (WiSNet)*, California, USA, January 2018, pp. 5–7.
- [41] M. Badi, J. Wensowitch, D. Rajan, and J. Camp, "Experimental evaluation of antenna polarization and elevation effects on drone communications," in *Proc. Int. ACM Conf. Modeling, Analysis Simulation Wireless Mobile Syst.*, Miami, USA, November 2019, pp. 211–220.
- [42] —, "Experimentally analyzing diverse antenna placements and orientations for uav communications," *IEEE Trans. Vehi. Technol.*, vol. 69, no. 12, pp. 14989–15004, 2020.
- [43] V. Semkin, S. Kang, J. Haarla, W. Xia, I. Huhtinen, G. Geraci, A. Lozano, G. Loiano, M. Mezzavilla, and S. Rangan, "Lightweight UAV-based measurement system for air-to-ground channels at 28 GHz," in *Proc. IEEE Annual Int. Symp. Personal, Indoor, Mobile Radio Commun. (PIMRC)*, September 2021, pp. 848–853.
- [44] R. Sun, D. W. Matolak, and W. Rayess, "Air-ground channel characterization for unmanned aircraft systems—Part IV: Airframe shadowing," *IEEE Trans. Vehi. Technol.*, vol. 66, no. 9, pp. 7643–7652, 2017.
- [45] S. S. Szyszkowicz, H. Yanikomeroglu, and J. S. Thompson, "On the feasibility of wireless shadowing correlation models," *IEEE Trans. Vehi. Technol.*, vol. 59, no. 9, pp. 4222–4236, 2010.
- [46] S. J. Maeng, O. Ozdemir, I. Guvenc, M. Sichitiu, and R. Dutta, "LTE I/Q measurement by AERPAAW platform for air-to-ground propagation modeling," *IEEE Dataport*, 2022. [Online]. Available: <https://dx.doi.org/10.21227/0p43-0d72>
- [47] S. Masrur, O. Ozdemir, A. Gurses, I. Guvenc, M. L. Sichitiu, R. Dutta, M. Mushi, h. Zajkowski, C. Dickerson, G. Reddy, S. V. Villar, C.-W. Wong, B. Chatterjee, S. Chaudhari, Z. Li, Y. Liu, P. Kudyba, H. Sun, J. S. Mandapaka, K. Namuduri, W. Wang, and F. Fund, "Collection: UAV-based RSS measurements from the AFAR challenge in digital twin and real-world environments," *IEEE Data Descrip.*, 2025.
- [48] C. Dickerson, A. H. Fahim Raouf, O. Ozdemir, I. Guvenc, and M. Sichitiu, "AERPAAW UAV-based signal data collected at varying altitudes and sampling rates for wireless communication studies," *IEEE Dataport*, 2024. [Online]. Available: <https://doi.org/10.5061/dryad.2z34tmpvv>
- [49] V. Marojevic, I. Guvenc, R. Dutta, M. L. Sichitiu, and B. A. Floyd, "Advanced wireless for unmanned aerial systems: 5G standardization, research challenges, and AERPAAW architecture," *IEEE Vehi. Technol. Mag.*, vol. 15, no. 2, pp. 22–30, 2020.
- [50] A. Gurses, G. Reddy, S. Masrur, O. Ozdemir, I. Guvenc, M. L. Sichitiu, A. Sahin, A. Alkhateeb, M. Mushi, and R. Dutta, "Digital twins and testbeds for supporting AI research with autonomous vehicle networks," *IEEE Commun. Mag.*, vol. 63, no. 4, pp. 56–62, 2025.
- [51] Octane Wireless, "SA-1400-5900 Data Sheet." [Online]. Available: <https://www.octanewireless.com/product/sa-1400-5900-tri-band-stub-antenna/>
- [52] I. Mobile Mark, "RM-WB1 series radiation pattern." [Online]. Available: [Online]. Available: <https://www.mobilemark.com/product/rm-wb1/>
- [53] A. Gurses, A. H. Fahim Raouf, S. J. Maeng, O. Ozdemir, I. Guvenc, and M. Sichitiu, "AERPAAW Find-a-Rover (AFAR) Challenge in December 2023," *IEEE Dataport*, 2024. [Online]. Available: <https://doi.org/10.5061/dryad.18931zd4g>
- [54] H. Wackernagel and H. Wackernagel, "Ordinary kriging," *Multivariate Geostatistics: An Introduction with Applications*, pp. 79–88, 2003.
- [55] R. A. Olea and R. A. Olea, "Simple kriging," *Geostatistics for Engineers and Earth Scientists*, pp. 7–30, 1999.
- [56] N. Cressie, *Statistics for Spatial Data*. John Wiley & Sons, 2015.
- [57] R. A. Olea, "Fundamentals of semivariogram estimation, modeling, and usage," 1994.
- [58] G. Casella and R. L. Berger, *Statistical Inference*. Cengage Learning, 2021.
- [59] G. Shabat, "Matrix completion using nuclear norm, spectral norm or weighted nuclear norm minimization," 2024. [Online]. Available: <https://www.mathworks.com/matlabcentral/fileexchange/50056-matrix-completion-using-nuclear-norm-spectral-norm-or-weighted-nuclear-norm-minimization>
- [60] S. J. Maeng, O. Ozdemir, I. Guvenc, and M. Sichitiu, "3D antenna pattern measurement for AERPAAW experiments," *IEEE Dataport*, 2023. [Online]. Available: <https://dx.doi.org/10.21227/mma2-0t93>